



# Star–Disk Interactions in Multiband Photometric Monitoring of the Classical T Tauri Star GI Tau

Zhen Guo<sup>1,2</sup>, Gregory J. Herczeg<sup>1</sup>, Jessy Jose<sup>1</sup>, Jianning Fu<sup>3</sup>, Po-Shih Chiang<sup>4</sup>, Konstantin Grankin<sup>5</sup>, Raúl Michel<sup>6</sup>, Ram Kesh Yadav<sup>7</sup>, Jinzhong Liu<sup>8</sup>, Wen-ping Chen<sup>4</sup>, Gang Li<sup>3</sup>, Huifang Xue<sup>3</sup>, Hubiao Niu<sup>3,8</sup>, Annapurni Subramaniam<sup>9</sup>, Saurabh Sharma<sup>10</sup>, Nikom Prasert<sup>7</sup>, Nahiely Flores-Fajardo<sup>1,11</sup>, Angel Castro<sup>6,12</sup>, and Liliana Altamirano<sup>6,12</sup>

<sup>1</sup> Kavli Institute for Astronomy and Astrophysics, Peking University, Yi He Yuan Lu 5, Haidian District, Beijing 100871, People's Republic of China; [guozhen9057@hotmail.com](mailto:guozhen9057@hotmail.com)

<sup>2</sup> Department of Astronomy, School of Physics, Peking University, Yi He Yuan Lu 5, Haidian District, Beijing 100871, People's Republic of China

<sup>3</sup> Department of Astronomy, Beijing Normal University, Beijing 100875, People's Republic of China

<sup>4</sup> Graduate Institute of Astronomy, National Central University, No. 300, Zhongda Rd., Zhongli Dist., Taoyuan City 32001, Taiwan

<sup>5</sup> Crimean Astrophysical Observatory, pos. Nauchnyi, Crimea, 298409 Russia

<sup>6</sup> Instituto de Astronomía, Universidad Nacional Autónoma de México, Apartado Postal 877, C.P. 22800, Ensenada, B.C., México

<sup>7</sup> National Astronomical Research Institute of Thailand, Chiang Mai, 50200, Thailand

<sup>8</sup> Xinjiang Astronomical Observatory, Urumqi, Xinjiang 830011, People's Republic of China

<sup>9</sup> Indian Institute of Astrophysics, Koramangala, Bangalore 560 034, India

<sup>10</sup> Aryabhata Research Institute of Observational Sciences, Manora Peak, Nainital 263 002, India

<sup>11</sup> Instituto de Ciencias Nucleares, Universidad Nacional Autónoma de México. Cd. Universitaria, 04510 Ciudad de México, México

<sup>12</sup> Universidad Autónoma de Ciudad Juárez, Instituto de Ingeniería y Tecnología. 1210 Plutarco Elías Calles, 32310 Cd. Juárez, CH, México

Received 2017 September 7; revised 2017 November 11; accepted 2017 November 20; published 2018 January 5

## Abstract

The variability of young stellar objects is mostly driven by star–disk interactions. In long-term photometric monitoring of the accreting T Tauri star GI Tau, we detect extinction events with typical depths of  $\Delta V \sim 2.5$  mag that last for days to months and often appear to occur stochastically. In 2014–2015, extinctions that repeated with a quasi-period of 21 days over several months are the first empirical evidence of slow warps predicted by magnetohydrodynamic simulations to form at a few stellar radii away from the central star. The reddening is consistent with  $R_V = 3.85 \pm 0.5$  and, along with an absence of diffuse interstellar bands, indicates that some dust processing has occurred in the disk. The 2015–2016 multiband light curve includes variations in spot coverage, extinction, and accretion, each of which results in different traces in color–magnitude diagrams. This light curve is initially dominated by a month-long extinction event and a return to the unocculted brightness. The subsequent light curve then features spot modulation with a 7.03 day period, punctuated by brief, randomly spaced extinction events. The accretion rate measured from *U*-band photometry ranges from  $1.3 \times 10^{-8}$  to  $1.1 \times 10^{-10} M_{\odot} \text{ yr}^{-1}$  (excluding the highest and lowest 5% of high- and low- accretion rate outliers), with an average of  $4.7 \times 10^{-9} M_{\odot} \text{ yr}^{-1}$ . A total of 50% of the mass is accreted during bursts of  $> 12.8 \times 10^{-9} M_{\odot} \text{ yr}^{-1}$ , which indicates limitations on analyses of disk evolution using single-epoch accretion rates.

**Key words:** stars: pre-main sequence – stars: variables: T Tauri, Herbig Ae/Be

**Supporting material:** data behind figures

## 1. Introduction

Classical T Tauri stars (CTTSs) are low-mass young stars surrounded by an accretion disk. The stellar magnetic field truncates the disk at a few stellar radii and channels gas from the disk onto the star (e.g., Camenzind 1990; Koenigl 1991; Shu et al. 1994). The measured strengths and geometries of magnetic fields and the profiles of emission and absorption lines are consistent with expectations of the magnetospheric accretion model (e.g., Johns-Krull 2007; Donati & Landstreet 2009; Hartmann et al. 2016). Magnetohydrodynamic (MHD) simulations of the magnetospheric accretion suggest that the accretion flow may be either stable or unstable, depending on the accretion rate, the magnetic field strength and morphology, and the inclination angle between the stellar spin and magnetic dipole (e.g., Romanova et al. 2013; Blinova et al. 2016).

The photometric variability of T Tauri stars has been studied for decades (Wenzel 1969; Grinin 1988; Herbst et al. 1994; Bouvier et al. 2013; Cody et al. 2017). When star–disk interactions are steady, an accretion column and the associated inner disk warp rotate around the star, periodically occulting the central star (e.g., Bouvier et al. 2007; McGinnis et al. 2015). In non-steady accretion, these extinction events may appear more stochastically and last for days, months, or even years. The obscure dust is located in a persistent puffed-up disk and inner rim (Dullemond et al. 2003; Ke et al. 2012), a warp induced by binarity (Hamilton et al. 2001), a disk instability at larger distances (Zhang et al. 2015), or perhaps even a non-axisymmetric bridge that links an inner disk with an outer disk (Loomis et al. 2017). The changes in the height of the inner disk have also been seen in anticorrelated variability of near- and mid-IR disk emission (Espaillat et al. 2011), with a possible relationship to accretion rate (Ingleby et al. 2015). The disk interpretation is challenged in one case (J1604–2130) by the measurement of a face-on inclination of an outer disk (Ansdell et al. 2016a). In a second case (RW Aur), the occultation source is uncertain and may be a dusty wind



Original content from this work may be used under the terms of the [Creative Commons Attribution 3.0 licence](https://creativecommons.org/licenses/by/3.0/). Any further distribution of this work must maintain attribution to the author(s) and the title of the work, journal citation and DOI.

(Petrov et al. 2015; Schneider et al. 2015b), a tidal encounter of the secondary star (Dai et al. 2015), the combination of occultation and time-variable accretion (Takami et al. 2016), or partial occultation of the inner disk (Facchini et al. 2016).

In this paper, we focus on short- and long-term extinction events detected in one CTTS, GI Tau. Stars with short-duration (1–5 days) extinction events, called dippers, are obscured by dust structures at or near the disk truncation radius (e.g., Alencar et al. 2010; Cody et al. 2014; Scaringi et al. 2016). AA Tau is the historical prototype for dippers (e.g., Bouvier et al. 1999, 2003). Periodic and quasi-periodic dippers have a periodicity distribution consistent with the distributions of stellar rotations (Cody et al. 2014). Long-term extinction events, called faders, occur when the star is occulted by disk components for weeks to years (e.g., Bouvier et al. 2013; Findeisen et al. 2013; Rodriguez et al. 2015, 2016b; Loomis et al. 2017); KH 15D is the prototype for faders (Hamilton et al. 2001). Some stars, including AA Tau, have exhibited both types of extinction events. Deep extinction events have also been called Type III variables or UXors (Herbst et al. 1994), especially when the occulted object is a Herbig AeBe star (e.g., Grinin et al. 1994; Natta et al. 1997).

In the midst of this extinction variability, emission is also always changing because of unstable accretion and spot rotation. Accretion variability is common in young stellar objects, as 10% of CTTSs have similar bursty light curves (Findeisen et al. 2013; Cody et al. 2014, 2017; Stauffer et al. 2014). The variable accretion process appears as changes in excess continuum and line emission above the photosphere (e.g., Alencar et al. 2012; Fang et al. 2013; Costigan et al. 2014), and the corresponding changes in photometry (Venuti et al. 2014; Sousa et al. 2016; Stauffer et al. 2016; Tofflemire et al. 2017a) are driven by either unsteady star-disk connections (e.g., Romanova et al. 2013) or changes in the disk density at the inner rim (Robinson et al. 2017). Spot modulation is also commonly seen among young stars with typical variations of  $\Delta V \lesssim 0.5$  mag (e.g., Herbst et al. 1994; Grankin et al. 2007), although spots in light curves of some CTTSs can be difficult to distinguish from extinction and accretion variations. Extinction, accretion, and spot variability each have particular patterns in high time-resolution photometry (Alencar et al. 2010, 2012; Morales-Calderón et al. 2011; Cody et al. 2017), multiband photometry (Herbst et al. 1994; Grankin et al. 2007; Venuti et al. 2015), and spectroscopic monitoring (Bouvier et al. 2007).

In this paper, we describe and analyze the multiband optical monitoring of the CTTS GI Tau obtained over two years. Our work provides a method to identify the variation mechanisms using the color information and to probe the star-disk interaction at the inner edge of the circumstellar disk. The paper is organized as follows. In Section 2, we describe our observation and data reduction. The photometric results and periodicity analysis are described in Section 3. In Section 4, we analyze this photometric variability in terms of the warp size and changes in accretion.

## 2. Observations

### 2.1. Properties of GI Tau

GI Tau is a Classical T Tauri star associated with the B18 cloud in the Taurus star-forming region (Myers 1982; Kenyon et al. 2008) and is separated by 13 arcsec from a wide

companion, GK Tau (Figure 1; see also, e.g., Kraus & Hillenbrand 2009). GI Tau has a circumstellar disk (e.g., Kenyon & Hartmann 1995; Luhman et al. 2010; Rebull et al. 2010) and ongoing accretion (e.g., Valenti et al. 1993; Gullbring et al. 1998). The average VLBI parallax distance of 140 pc to the Taurus star-forming region (Loinard et al. 2007; Torres et al. 2009, 2012) is adopted as the distance to GI Tau.

Companion searches with high-resolution near-IR imaging (e.g., Daemgen et al. 2015) and high-resolution spectroscopy (Nguyen et al. 2012) have yielded non-detections, indicating that GI Tau is likely a single star. A  $\sim 7$  day period has been detected in some epochs (Vrba et al. 1986; Herbst et al. 1994) but is absent in other epochs (e.g., Grankin et al. 2007; Rodriguez et al. 2017a), perhaps because spot changes may be masked by complications in the light curve from extinction and accretion variability.

The estimated spectral type of GI Tau ranges from K5–M0.5 (Rydgren et al. 1976; Herbig 1977; Cohen & Kuhl 1979; Hartigan et al. 1994; Taguchi et al. 2009; Herczeg & Hillenbrand 2014), with differences caused by methodology and a non-uniform temperature distribution on the stellar surface (see, e.g., Gully-Santiago et al. 2017). Extinction events have been previously detected from photometry (Herbst et al. 1994; Grankin et al. 2007; Rodriguez et al. 2016a). In three optical spectra, Herczeg & Hillenbrand (2014) found that fixing the spectral type to a single value required an extinction that varied from  $A_V = 1.05$  to 2.55 mag. Our analysis in Section 4.3 indicates a minimum  $A_V = 0.75$ –1.0 mag, which is likely interstellar; any additional extinction is likely caused by the disk.

Adopting a spectral type of M0.4 ( $T_{\text{eff}} = 3828$  K) and  $\log(L/L_{\odot}) = -0.25$  (Herczeg & Hillenbrand 2014; see also Grankin 2016), the mass and age are  $0.53 M_{\odot}$  and 1.4 Myr as inferred from the pre-main-sequence evolutionary tracks of Baraffe et al. (2015), and  $0.92 M_{\odot}$  and 4 Myr from the magnetic tracks of Feiden (2016). These parameters are sensitive to the unknown spot properties of the star (Gully-Santiago et al. 2017). However, dynamical masses measured from disk rotation around stars of similar spectral types lead to masses of  $0.60$ – $0.95 M_{\odot}$  (Simon et al. 2017).

The disk inclination has not been measured. Given a radius  $R = 1.7 R_{\odot}$ , rotational period  $P_{\text{rot}} = 7.03 \pm 0.02$  day (see Section 3.1), and stellar rotational velocity  $v \sin i = 12.7 \pm 1.9$  km s $^{-1}$  (Nguyen et al. 2009), the stellar inclination is  $>60^{\circ}$  (see also Johns-Krull & Valenti 2001). Broad redshifted absorption in He I  $\lambda 10830$  has a similar profile as that seen in AA Tau (Fischer et al. 2008) and supports this high inclination.

### 2.2. SNIFS Photometry and Spectroscopy

We obtained spectra and photometry of GI Tau with the Super-Nova Integral Field Spectrograph (SNIFS; Aldering et al. 2002; Lantz et al. 2004) from 2014 November 26 to December 15. SNIFS is an Integral Field Spectrograph on the UH 88 inch telescope on Maunakea that produces  $R \sim 1000$  spectra from 3200 to 10,000 Å over a  $6'' \times 6''$  field of view (FOV). Short acquisition images were obtained with a  $9/6 \times 9/6$  FOV imager with a V-band filter and are used here for photometry.

The full set of our SNIFS observations include spectroscopic monitoring of  $\sim 30$  CTTSs. GI Tau was initially selected as a target based on past identification of extinction events (see,

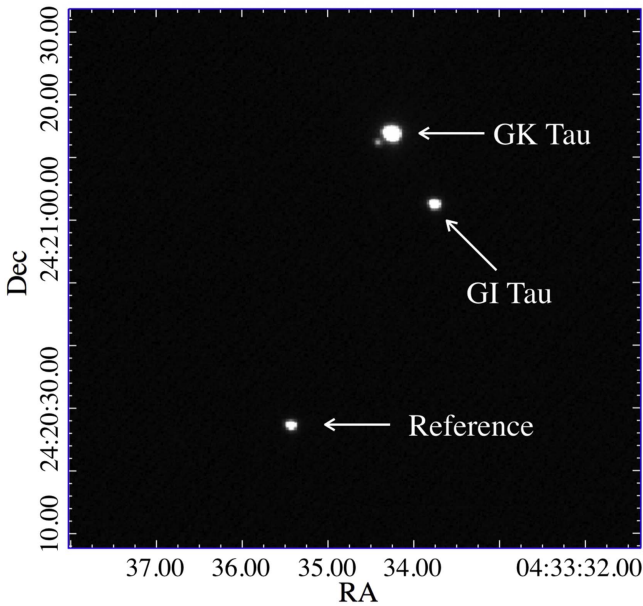


**Figure 1.** V-band image of GI Tau and GK Tau obtained using SNIFS at the UH88 telescope. GI Tau, GK Tau and its close visual companion, and one of the reference stars are marked in the image.

e.g., Grankin et al. 2007; Herczeg & Hillenbrand 2014). We detected a deep extinction event at the beginning of our SNIFS campaign and decided to intensively monitor GI Tau for the remainder of our campaign. Two spectra from this spectroscopic monitoring campaign are analyzed in this paper (see Section 2.5).

### 2.3. Subsequent Photometric Campaigns (2014–2016)

Following our SNIFS photometry, we monitored GI Tau from 2014 to 2016 with 11 other telescopes. The details of the telescopes, instruments, and observations are described in Table 1. The complete set of photometry is listed in an online table.

From 2014 December 16 (MJD 57007) until 2015 March 25 (MJD 57108), photometry was obtained in the V-band filter with a cadence of one to two visits per night. From 2015 October–2016 February, multiband photometry was obtained in the B, V, R, and I bands, and in U when available. Different observational strategies were set based on the time allowance of each telescope. SLT, the 1 m Thailand Southern Telescope, and the 1.3 m JCBT observed the selected field one to three times on each clear night. The 0.5 m telescope at TNO and 2 m HCT also contributed weeks-long observations. The NOWT (Liu et al. 2014) and NBT monitored GI Tau for 4–6 hr for seven and three consecutive nights, respectively, to measure variations on short timescales.

### 2.4. Data Reduction of Photometry

The data were reduced with custom-written routines in IDL. The images were corrected for detector bias, flat-field, and cosmic rays. The stellar brightnesses of GI Tau, GK Tau, and many field stars in the frame are measured with aperture photometry. For field stars, the sky background is measured in an annulus with an 8 arcsec inner radius and 10 arcsec outer radius around the star. Since the distance between GI Tau and GK Tau is only 13.2 arcsec, the background levels are adopted

directly from the sky background of the nearby reference star. The counts for each star are then extracted using a radius equal to two times the seeing (in FWHM), with an upper limit on the radius of  $6''.5$  arcsec. Photometry with fixed apertures of  $1''$ ,  $3''$ , and  $6''$  and PSF fitting yield results that are generally consistent with our approach, but with larger standard deviations in the photometry.

Four bright stars are identified as non-variables (Figure 2) and are selected as reference stars to calibrate the BVR photometry of GI Tau. The measured standard deviations of all reference stars are 0.017 mag in I, 0.028 mag in V, and 0.042 mag in the B band, after excluding the images obtained during the full moon. The measurements are less reliable ( $\Delta I > 0.05$  mag) in observations with seeing larger than  $4''$ . The number of reference stars used for each telescope depends on the FOV and is listed in Table 1.

In U-band observations, only one field star, with  $m_U = 13.50$  mag,<sup>13</sup> located within the  $10' \times 10'$  FOV is bright enough to be used as a calibrator. Unsaturated images in the B, V and I bands indicate that this calibrator is not variable. The accuracy of our U-band observations is typically limited to  $\sim 0.05$  mag by the signal-to-noise ratio of GI Tau. The differential effects of telluric absorption versus airmass are not corrected.

A reflection nebulosity around GI Tau and GK Tau (Arce & Sargent 2006) is detected in stacked images, with a surface brightness of  $I = 22.8$  mag arcsec<sup>-2</sup> and  $B = 25.5$  mag arcsec<sup>-2</sup>. The flux contribution from the nebulosity within a  $6''.5$  radius aperture is 17.5 mag in the I band and 20.2 mag in the B band, or  $\sim 4$  mag fainter than the faintest measurements of GI Tau. Compared with the photometric accuracy and variability of GI Tau, the differential flux contribution from the nebulosity introduced by using different aperture sizes is negligible.

For absolute photometric calibration, we observed the GI Tau field and the region PG 02331 from Landolt (1992) at a range of airmasses with the 2 m HCT on 2015 December 1. The atmospheric extinction and instrument coefficients are measured from PG 02331 and applied to bright stars in the GI Tau field. The standard magnitudes of these reference stars are then used to apply the zero-point shifts to each observation obtained by all other telescopes in this study.

The absolute photometric calibration accuracy should be  $\sim 0.02$  mag in the V and I bands and 0.05 mag in the B band, following the uncertainties in the Landolt star calibrations. However, an absolute offset of 0.09 mag in V-band calibration is identified when comparing our photometry to the historical photometry of Grankin et al. (2007; see Figure 5) and to the synthetic photometry obtained from our flux-calibrated SNIFS spectra. The source of this problem could not be identified. Our relative photometric calibration should be unaffected. The synthetic  $\Delta V$  between our SNIFS spectra is within 0.01 mag of the directly measured  $\Delta V$  obtained in our acquisition images.

### 2.5. Data Reduction of Spectroscopy

The SNIFS spectra of GI Tau and the spectrophotometric standard G191B2B (Oke 1990) were reduced with custom-written routines in IDL. The emission is split at  $\sim 5200$  Å by a dichroic into separate red and blue channels. The raw images consist of 225 separate spectra, each from a given spaxel in the

<sup>13</sup> This U-band measurement was measured by Audard et al. (2007) with the XMM-Newton Optical and UV Monitor ( $U_{OM}$ ). With a spectral type of B8, the offset between the  $U_{OM}$  and Johnson U system of  $U - U_{OM} \sim -0.02$  is small and is ignored in our analysis.

**Table 1**  
Summary of Observations

Telescope	Location	Diameter (m)	Pix Size (")	Field of View	No. Ref	Filter	Nights of Obs.	No. Visits/Night
2014–2015								
UH88	Maunakea, Hawaii	2.2	0.27	9'3 × 9'3	2	V	18	1–6
YNAO	YNAO, China	1	0.41	7'3 × 7'3	2	V	4	4
AZT-11	CrAO, Russia	1.25	0.62	10'6 × 10'7	3	V	6	1
OAN-SPM (0.84)	SPM, Mexico	0.84	0.44	7'6 × 7'6	4	VR	4	2 hr <sup>a</sup>
HCT	Hanle, India	2	0.30	10'2 × 10'2	4	V	23	1
2015–2016								
OAN-SPM (1.5)	SPM, Mexico	1.5	0.32	5'4 × 5'4	1	VI	34	2 hr <sup>a</sup>
HCT	Hanle, India	2	0.30	10'2 × 10'2	4	UVI	23	1–3
SLT	Lulin, Taiwan	0.40	0.78	26'8 × 26'8	4	UBVI	74	1–3
NOWT	XAO, China	1	1.13	1'3 × 1'3	4	BVRI	5	>5 hr <sup>a</sup>
JCBT	VBO, India	1.3	0.24	16'5 × 8'6	4	BVI	20	1
TST	CTIO, Chile	0.6	0.63	22' × 22'	4	BVRI	45	1
NBT	Xinglong, China	0.85	0.91	30' × 30'	4	UBVRI	10	>5 hr <sup>a</sup>
TNO	TNO, Thailand	0.5	0.63	21'5 × 21'5	4	BVI	21	1–2

**Note.** UH88: University of Hawaii 2.2 m telescope. YNAO: 1 m RCC telescope at Yunnan Astronomical Observatory, Kunming, China. AZT-11: 1.25 m telescope at Crimean Astronomical Observatory, Russia. OAN-SPM: 0.84 m and 1.5 m telescopes at Observatorio Astronomico Nacional, Sierra San Pedro Mártir, Mexico. HCT: 2 m Himalayan Chandra Telescope at Indian Astronomical Observatory, Hanle (Ladakh), India. SLT: 40 cm telescope at Lulin Observatory, Taiwan. NOWT: Nanshan One meter Wide-field Telescope at Xinjiang Astronomical Observatory, Urumqi, China. JCBT: 1.3 m J.C. Bhattacharya Telescope at Vainu Bappu Observatory, Kavalur, India. TST: 0.6 m Thai Southern Hemisphere Telescope (PROMPT-8), operated by the Skynet Robotic Telescope Network, at the Cerro Tololo Inter-American Observatory, Chile. NBT: 85 cm reflection telescope at Xinglong Station of the National Astronomical Observatories of China. TNO: 0.5 m telescope at Thai National Observatory, National Astronomical Research Institute of Thailand (NARIT).

<sup>a</sup> Represents consecutive observation for X hours.

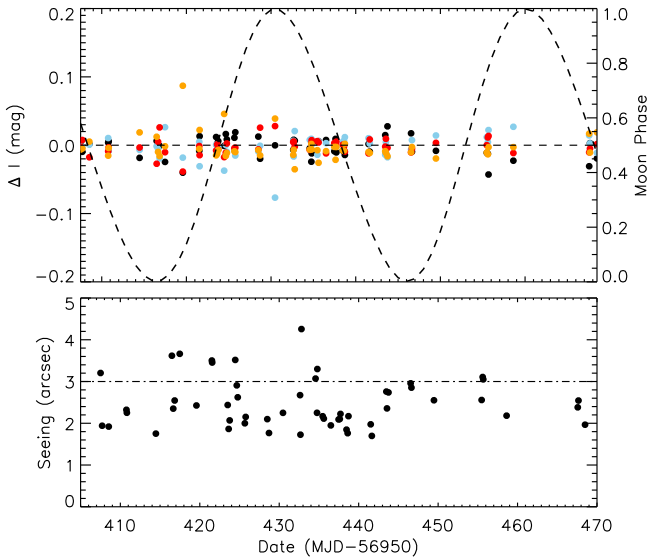


**Figure 2.** Top: accuracy of the *I*-band photometric calibration of the four reference stars (separated by different colors) taken by SLT, plotted as the difference between each observation and the median magnitude,  $\Delta I$ . The standard deviations of each reference stars are 0.016, 0.018, 0.013, and 0.018 mag. The lunar phase is shown by a dashed black curve. Bottom: the seeing during each observation, with the horizontal dotted–dashed line indicating 3".

15 × 15 integral field unit. The counts in each spectrum are extracted by fitting a cross-spectrum profile, measured from flats, to each wavelength pixel. The spectra in each spaxel was then wavelength-calibrated to  $\sim 10 \text{ km s}^{-1}$  using arc lamps, flat-corrected in each spaxel, and then regridded onto the same wavelength scale.

The final spectra are extracted from the data cube by fitting a 2D profile and sky background at each wavelength bin. The

spectra of GI Tau were then flux-calibrated using G191B2B spectra obtained within 1 hr of GI Tau. The average airmass correction was calculated using spectra of G191B2B over the 20 night run and was then applied to each epoch. Two spectra were selected for use in this paper because they were obtained in photometric conditions, near in time to the photometric calibrators, and at the local minimum and maximum of the light curve.

### 3. Results and Analysis

In the 2014–2015 light curve of GI Tau, the most prominent features are several extinction events with depths of  $\Delta m_V > 2.5$  mag and durations of three to five days (see Figure 3). The 2015–2016 light curve of GI Tau began with a dim epoch that lasted  $\sim 50$  days, followed by a period with smaller periodic brightness variations (Figure 4).

These photometric variations are summarized by the color–color and color–magnitude diagrams in Figure 5. The *V*-band brightness varied by 2 mag, the *V* – *I* color by 0.8 mag, and the *B* – *V* color by 0.5 mag. The locus of points on the color–magnitude diagram is similar to that seen in the long-term monitoring of GI Tau by Grankin et al. (2007), except for the offset in the *V* band discussed in Section 2.4.

In faint epochs, a “blue turnaround” is seen, in which the color variation is achromatic with further dimming of *V*. This blue turnaround, also seen in AA Tau (Bouvier et al. 1999) and other CTTSs (Grankin et al. 2007), is likely caused by an increased importance of the scattered light, since stars with edge-on disks typically appear blue at optical wavelengths (e.g., Padgett et al. 1999; Herczeg & Hillenbrand 2014). These epochs are ignored when calculating accretion rates. However, if the bluer colors are caused by higher accretion rates during these faint epochs, then this choice would bias our results.

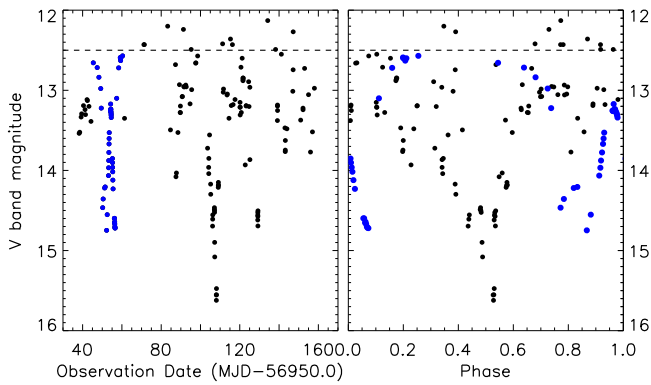


**Figure 3.** *V*-band light curve of GI Tau during 2014–2015 vs. time (left) and phase-folded for the  $\sim 21$  day period (right) and binned to 30 minute intervals where relevant. A “double dip” feature from days 45 to 61 is shown by the blue dots. The horizontal dashed line is the approximate baseline of GI Tau used here to calculate the occultation depth. The data used to create this figure are available.

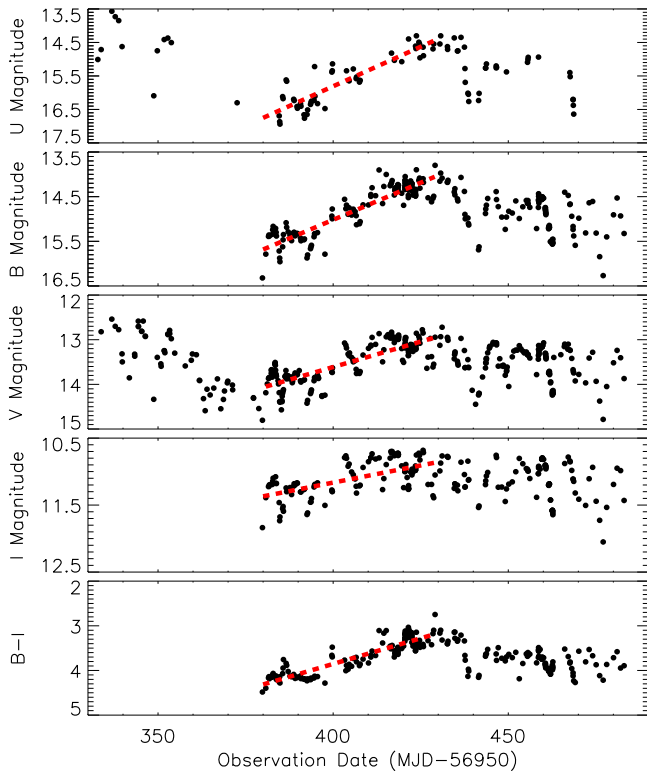


**Figure 4.** From top to bottom, the *U*, *B*, *V*, and *I* bands and *B* – *I* light curves of GI Tau during the 2015–2016 campaign. The general brightening that occurred from day 380 is fit with the red dashed lines. The data used to create this figure are available.

In this section, we describe how the light curves are combined with the color–color and color–magnitude diagrams are used to identify variability caused by stellar spots, circumstellar extinction events, and accretion bursts.

### 3.1. Spot Modulation in 2015–2016

Periodicity in the 2015–2016 light curve is most prominent in the *I* band. The Generalized Lomb–Scargle (GLS) periodogram (Zechmeister & Kürster 2009) of the *I*-band light curve

yields a best-fit period of  $7.03 \pm 0.02$  days, with the error bar adopted from the FWHM of the periodogram profile (Figure 6). Prior to the fit, the long-term trends were approximated as a third-order polynomial and were removed from the data (Zajtseva 2010). Fitting parameters to the *B*-, *V*-, and *I*-band light curves are shown in Table 2.

The sinusoidal morphology of the phase-folded light curves indicates the presence of a single large spot, similar to some other young stars with similar spectral types (e.g., Alencar et al. 2010; Rebull et al. 2016; Gully-Santiago et al. 2017). The standard deviation of the residual of 0.11 mag is likely caused by extinction and accretion events (discussed in Sections 3.2–3.4). The power of the periodogram,  $\zeta = p_{\max}/\sigma_p$ , is highest in the *I* band, since the other bands are more sensitive to accretion and extinction variations. The variations in the colors are synchronous (Figure 7).

False-alarm probabilities<sup>14</sup> for the period are computed using a Fisher randomization test with input periods between 2 and 100 days (e.g., Linnell Nemec & Nemec 1985). The 7.03 day period exceeds the 99% confidence level. This period is consistent with past measurements of the photometric period. In other epochs, including our monitoring in 2014–2015 and the 2008–2014 light curves described by Rodriguez et al. (2017b), any modulation from spots is masked by the much stronger variability caused by extinction.

### 3.2. Extinction Events in 2014–2015

Several photometric dips are shown in the *V*-band light curve of the 2014–2015 campaign, with depths of 1.5–3.1 mag relative to the out-of-extinction brightness of  $\sim 12.5$  mag and durations of 3–5 days (see list of extinction dips in Table 3).

The light curve of GI Tau reveals a wide range of durations and frequencies of extinction events. Our initial SNIFS monitoring included a double-dip extinction event, during which the *V*-band emission from the star faded, brightened, and then quickly faded again. The separation of the two minima is 5 days, and the total combined duration is 11 days, longer than one stellar rotation period. The  $R_V$  measurement based on spectra will be discussed in Section 4.2.

Subsequent follow-up photometry over the next months led to the detection of four dips with  $A_V > 1.5$  mag (see Table 3). These dips have a centroid time that repeats with a  $\sim 21$  day period. However, the preceding double-dip is inconsistent with this quasi-period. The extinctions that occur in the following year, described below, are also inconsistent with any periodicity.

### 3.3. Extinction Events in 2015–2016

The light curve during our 2015–2016 campaign is initially dominated by a gradual fade that reaches  $\Delta V = 1.5$  mag and then returns to the bright state, in total covering a period of  $\sim 80$  days (Figure 4). In addition to this months-long fading event, several small and large photometric dips are detected with

<sup>14</sup> False-alarm probabilities are the fraction of permutations (i.e., shuffled time series) that include a peak higher than that of the periodogram of the unrandomized data set at any frequency. This therefore represents the probability that, given the frequency search parameters, no periodic component is present in the data with this period. To ensure reliable significance values, the number of permutations was set to 1000. If the false alarm probabilities lie between 0.00 and 0.01, then the quoted period is a correct one with 95% confidence. The periodogram is computed at 5000 frequencies between 0 and  $0.5 \text{ day}^{-1}$ .

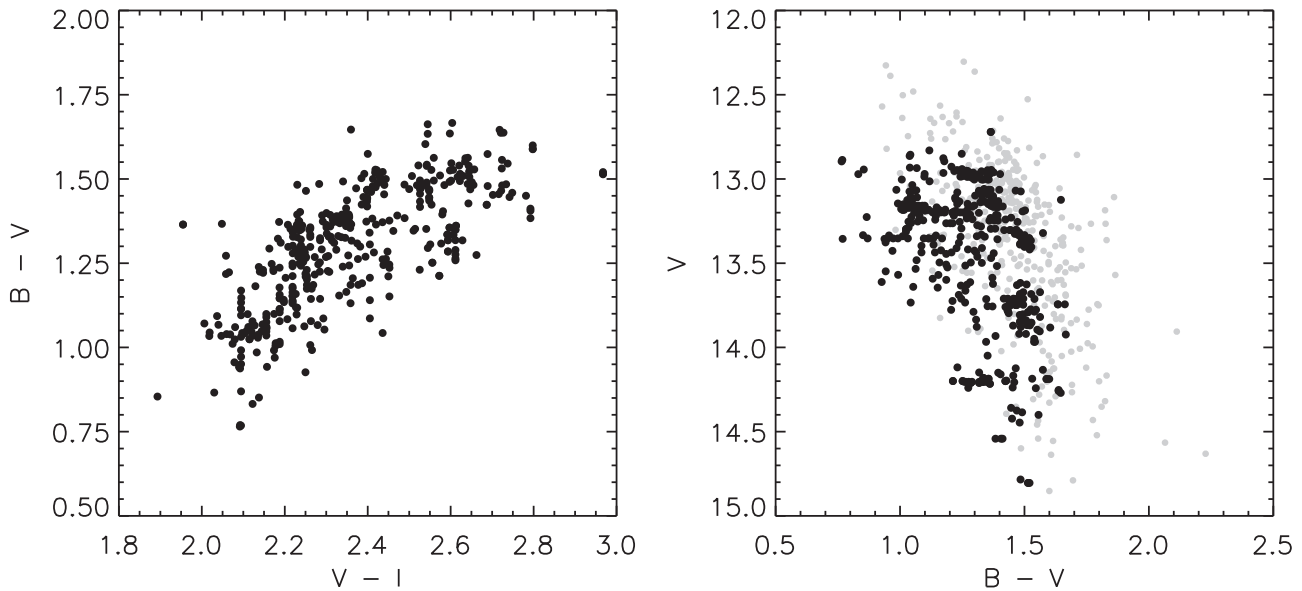


**Figure 5.** Color-color and color-magnitude diagrams of GI Tau during the 2015–2016 observation campaign, with data in our work shown by the black dots and archival data from Grankin et al. (2007) shown by the gray dots.

durations of 3–8 days, after correcting for spot-induced periodicity (see Figures 4 and 8 and Table 3).

Figure 4 shows a brief ( $\sim 3$  day) dip in the spot-corrected light curve at day 397, with a depth of  $\Delta I = 0.39$  mag,  $\Delta V = 0.45$  mag, and  $\Delta B = 0.56$  mag. A deeper and longer dip occurred around day 440, lasting for  $\sim 8$  days (Figure 8). Gaussian fits to the dips, as measured after accounting for spot rotation, yield  $A_I = 0.60$  mag,  $A_V = 1.22$  mag, and  $A_B = 1.56$  mag, and FWHMs of 3.73, 3.52, and 3.76 days, respectively. In those fits, the depths are measured relative to the post-dip light curve, which is well fit by a sine curve. There is no obvious periodicity of this extinction event.

### 3.4. Short Timescale Bursts

Photometry in the  $U$  and  $B$  bands is more sensitive to accretion than photometry with longer wavelength filters. At short wavelengths, the photospheric emission of GI Tau is faint relative to the continuum emission produced by the accretion shock (see the review by Hartmann et al. 2016). In our monitoring, the  $U$  and  $B$  bands exhibit stronger variations than the  $V$  and  $I$  bands.

Our campaign included five nights with constant monitoring of GI Tau on NOWT, during which several short bursts occurred (see Table 4 and Figure 9). The largest burst in  $B$ , detected during the first night, reached a peak of  $\Delta B \sim 0.3$  mag and lasted  $\sim 3.5$  hr. Four other shorter, smaller bursts are detected in the last two days. The average duration of these five bursts detected by NOWT is  $\sim 1.7$  hr, and the maximum amplitude in the  $B$  band is 0.31 mag. The changes in the brightness caused by these accretion bursts are an order of magnitude smaller than those caused by the deep extinctions. The corresponding increases of accretion rate during these bursts are calculated in Section 4.3. In one case, the  $B$ -band brightness is consistent with a non-detection, so the minimum and maximum accretion rates before and during the burst are not reported. These short bursts are attributed here to accretion but could alternatively be attributed to stellar flares (e.g., Kowalski et al. 2016; Tofflemire et al. 2017a, 2017b).

### 3.5. Color Analysis

Variable extinction, accretion, and spot coverage are all identified from the optical light curve of GI Tau. The traces of different phenomena in the color-magnitude diagrams can be used to distinguish the variation mechanisms. In this section, we describe the different signatures that changes in each of these properties imprint on the color-color and color-magnitude diagrams (Figure 10).

The short extinctions dips in the 2015–2016 campaign exhibit similar changes in the color-magnitude diagram with  $\Delta V = 2.10 \pm 0.08 \Delta(V - I)$  and  $\Delta I = 0.7 \pm 0.1 \Delta(B - I)$ . The long-term variation seen in the first half of the 2015–2016 campaign appears similar to the dips and is also attributed to extinction. These empirical relationships are consistent with expectations for dust reddening. The accretion bursts appear as horizontal changes in  $B - I$  versus  $I$ , indicating that the accretion only has a minor effect on the  $I$ -band brightness and that the  $B - I$  color is a good tracer of accretion. In this case, accretion is much flatter than extinction in the  $I$  versus  $B - I$  diagram (Figure 10 and Table 5). Venuti et al. (2015) obtained similar results in two weeks of monitoring young stars in NGC 2264 with CFHT in the  $u'$  and  $r$  bands.

As the spot rotates, the  $V - I$  colors change by 0.06 mag while the  $B - V$  colors change by 0.08 mag. These small color changes during spot modulation are consistent with those of the weak-line T Tauri star LkCa 4 during three decades of photometry (Grankin et al. 2008; Gully-Santiago et al. 2017). The locus that spot modulation traces on the color-magnitude diagrams has a slope between that of accretion and extinction. However, since the spot modulation has a unique periodicity, the spot information is readily extracted from a frequency analysis.

Pre-main-sequence stellar evolution tracks from Baraffe et al. (2015) are also presented in the color-magnitude diagrams, with colors adopted from Allard (2014). In distant clusters, properties of low-mass stars are often inferred from photometry (e.g., Reggiani et al. 2011; Jose et al. 2016; Beccari et al. 2017). Extinction events, accretion bursts, and spots each influence the inferred mass and age of member stars. Extinction

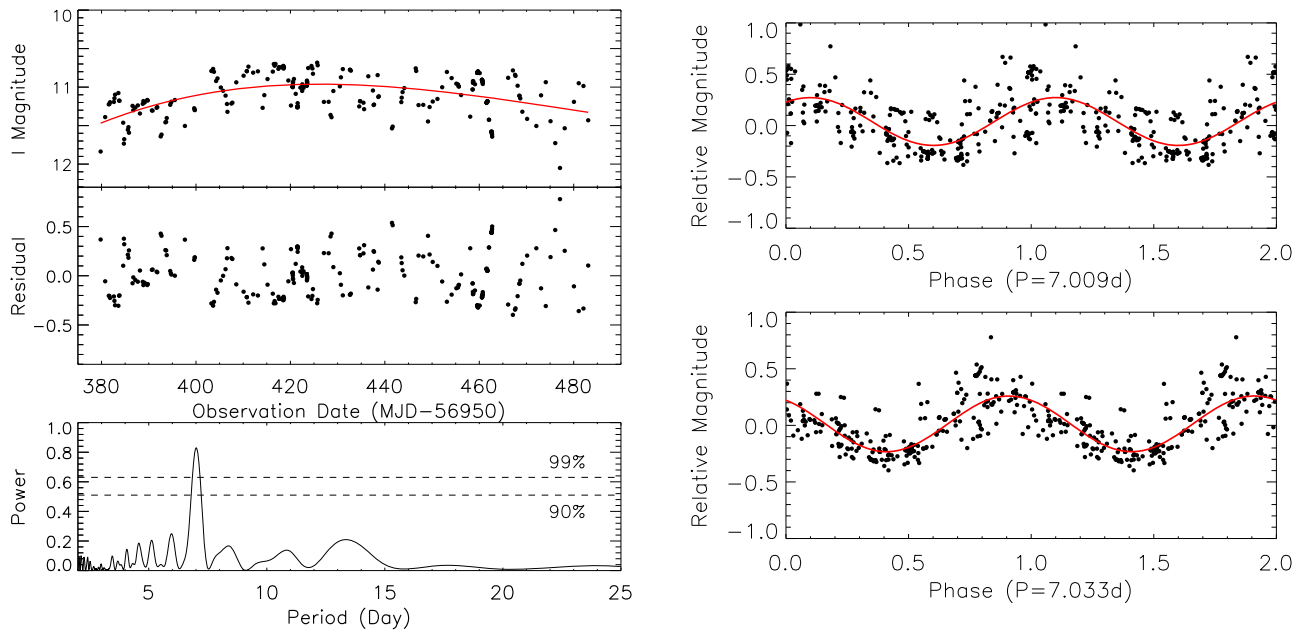


**Figure 6.** Top left: the  $I$ -band light curve of GI Tau, with a red line showing a third order polynomial fit to long-term variations. Middle left: the residual of the fit from the upper panel. Bottom left: the periodogram calculated from the light curve in the middle panel, showing a peak at 7.03 days. Top right: phase-folded  $I$ -band light curve in campaign 2015–2016 using the raw data from the top-left panel. Bottom right: phase-folded  $I$ -band light curve by the residuals from the left-middle panel.

curves are parallel to the color isochrone of cool stars in the  $V-I$  versus  $V$  diagram, which indicate that the age determination from  $V$ - and  $I$ -band photometry is robust to extinction changes (see also discussion in Sicilia-Aguilar et al. 2005). The age of GI Tau inferred from the Baraffe et al. (2015) models is consistently between 1 and 2 Myr (see also the age estimation in Section 2.1). However, the  $V-I$  color range introduces uncertainty in the mass or  $T_{\text{eff}}$  estimates when analysis is restricted to photometry, with larger uncertainties when using non-simultaneous photometry.

#### 4. Discussion

Photometric dips, accretion bursts, and a 7.03 day periodicity all shape the light curve of GI Tau during our monitoring over two years. The properties of the inner edge of the circumstellar disk and the star-disk interactions can be determined from the morphology and color changes during the variation events. The existence of quasi-periodic extinctions in the first year and the non-detection during our second campaign, and the change in morphology and frequency of events within each campaign, indicate an evolution of the inner disk structure over at most a few orbital timescales. In this section, we discuss the 2014–2015 quasi-periodicity in terms of a warp model, the extinction curve, and the distribution of accretion rates.

##### 4.1. The Slow Warp Model for the Quasi-periodic Dips of 2014–2015

Emission from young stars is periodically occulted by the inner edge of the circumstellar disk, when the disk is viewed close to edge-on. The presence of asymmetric disk warps or puffed-up inner rims will extinct the stellar brightness (see, e.g., the radiative transfer simulations of Kesseli et al. 2016). Figure 11 presents the periods and amplitudes of extinction events seen in young stars. For most dippers, these occultations are thought to occur once per stellar period, last  $\sim 1$  day, and are caused by inner disk warps related to accretion funnel flows

(e.g., Bouvier et al. 2007; Romanova et al. 2013). For faders, the occultations are prolonged and may last months or even years. The GI Tau light curve exhibits some characteristics of both dippers and faders.

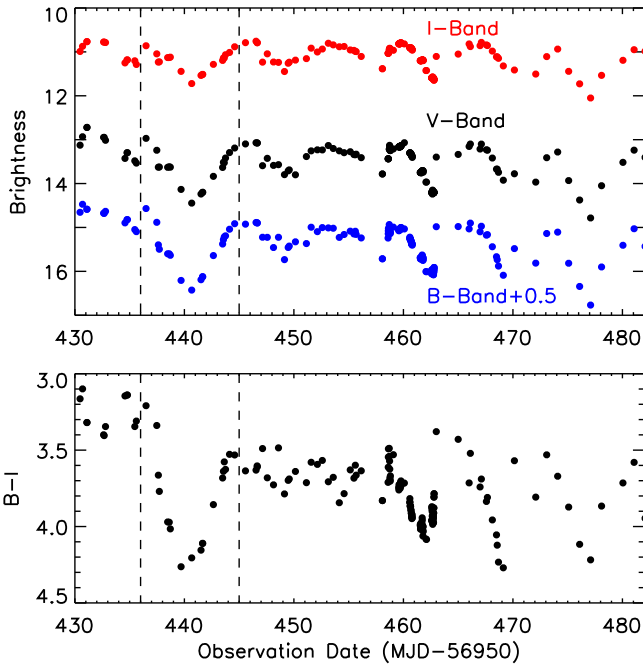
In the 2014–2015 monitoring, the (quasi)-periodic dips of 1.5–2.5 mag in  $V$  occurred every  $\sim 21$  days. In contrast, all previous periodic dippers have periodicity on much shorter timescales that are consistent with the stellar rotation period (Bouvier et al. 2007; Grankin et al. 2007; Alencar et al. 2010; McGinnis et al. 2015) and have depths of  $A_V = 0.1 - 1$  mag. The deep obscuration depth of GI Tau in this campaign is comparable to UXors, which are usually early-type PMSs undergoing variable extinctions with depths  $A_V > 1$  mag (Grinin et al. 1991, 1994; Herbst et al. 1994; Natta et al. 1997; Dullemond et al. 2003). However, no clear periodicity has been reported in UXors.

The deep events of GI Tau recur near every  $\sim 3$  stellar rotation periods and may be evidence of the slow warp in the MHD simulations of magnetospheric accretion by Romanova et al. (2013). In these simulations, two warps form in the circumstellar disk: a thin warp located at the co-rotation radius ( $R_{\text{cor}}$ ) and a thick warp outside of the co-rotation radius. Material can be trapped by the thick warp because of coupling between the stellar rotation and global oscillations in the disk. The thick warp is expected to rotate several times more slowly than the star, since it is located at a larger radii in the disk and also cause dips that are more optically thick than those in thin warps at the inner disk edge. The thick warp has a high scale height, so that it periodically intercepts our line of sight and causes extinction. Although this slow warp was quasi-periodic over  $\sim 60$  days, the feature was short-lived: it formed soon after our initial 20 night monitoring and had evolved or dissipated by the next year.

The  $\sim 80$  day long fade and return at the end of 2015 is much shorter than equivalent events in other stars, such as the years-long fading on AA Tau and V409 Tau (Bouvier et al. 2013; Rodriguez et al. 2015). The obscuration source may be an

**Table 2**  
Sine Fit Results

Parameters	$I+poly$	$I$	$V$	$B$
Period (days)	$7.03 \pm 0.02$	$7.01 \pm 0.03$	$7.09 \pm 0.08$	$7.20 \pm 0.09$
Frequency (1/day)	$0.1422 \pm 0.0004$	$0.1426 \pm 0.0006$	$0.140 \pm 0.002$	$0.139 \pm 0.002$
Maximum Power: $p_{max}$	0.829	0.417	0.645	0.567
Standard deviation: $\sigma_p$	0.037	0.022	0.078	0.110
Index: $p_{max}/\sigma_p$	21.82	18.77	8.26	5.15
Amplitude (mag)	$0.24 \pm 0.01$	$0.23 \pm 0.02$	$0.32 \pm 0.09$	$0.41 \pm 0.03$
rms of Residual (mag)	0.145	0.202	0.167	0.488

**Figure 7.** Top:  $B$ - (offset by 0.5 mag),  $V$ -, and  $I$ -band light curves of GI Tau between days 430–485, showing a combination of spots and occultations. Bottom: the  $B - I$  color, with large dips that indicate occultations.**Table 3**  
Extinction Events on GI Tau

Time (MJD-56950)	$V_{min}$ (mag)	$\Delta V$ (mag)	Duration (days)
50.2	14.34	1.84	5
56.5	14.72	2.22	4
87.5	14.07	1.57	>3
108.1	15.62	3.12	5
129.2	14.70	2.20	...
380.0	14.34	1.54	80
396.8	14.27	0.48	3
440.6	14.45	1.15	8
477.1	14.78	0.96	4

azimuthally symmetric warp located close to the inner edge of the disk (e.g., Dullemond et al. 2003), distant disk structures (e.g., Zhang et al. 2015), or a bridge between an outer and inner disk (Loomis et al. 2017).

As the obscuration source of the extinction dips is located not far from the inner edge of the circumstellar disk or the co-rotation and truncation radius, we calculate the co-rotation radius of GI Tau based on the stellar parameters and spin

period obtained from this work:

$$R_{cor} = (G M_* P_*^2)^{1/3} (2\pi)^{-2/3} = 7.35 R_* = 0.06 \text{ au}, \quad (1)$$

where  $M_* = 0.53 M_\odot$ ,  $R_* = 1.7 R_\odot$ , and  $P_* = 7.03$  days.

The morphology of the dips is related to the disk inclination, orientation of the magnetic field dipole, and warp opacity. The short durations of the dips detected in GI Tau indicates a moderate inclination viewing angle (Bodman et al. 2017). The shape of the dips depends on the ingress timescale, i.e., the timescale for the structure to move in front of the star. The orbital velocity is calculated by the duration of the ingress time following the equation

$$V_{orbit} \times \sin \theta = L/t_{ingress}, \quad (2)$$

where the definition of  $L$  is half of the angular size of the warp (Bouvier et al. 1999), and the  $t_{ingress}$  should be around half of the total obscuration time. As shown in Figure 8, the typical  $t_{ingress}$  is 4 days while the occultation lasts for 8 days. A disk warp located at  $\sim 1.5 R_{cor}$  has a local disk rotation velocity  $v_{rot} = 43.5 \text{ km s}^{-1}$ . A Gaussian shape warp modeled by Romanova et al. (2013) with  $v_{warp} = 0.25 v_{rot}$  should have a width  $L = 6.9 R_*$  in horizontal size for an 8 day duration.

The maximum observed duration of the dips in the 2014–2015 campaign is 5 days, or 25% of the occultation period ( $P \sim 20$  days). If we assume that the warp system is located at 1.2–1.5 co-rotation radius, as indicated by the Romanova et al. (2013) simulations, the angular width of the warp  $L$  is as large as  $2.35 R_{cor}$  or  $\sim 18.6 R_*$ . A hydrogen gas column density is derived by Bohlin et al. (1978):  $N_H/E(B - V) = 5.8 \times 10^{21} \text{ cm}^{-2} \text{ mag}^{-1}$ , assuming an  $R_V = 3.85$  extinction (see Section 4.2). We also assume an ISM gas-to-dust ratio of 100: 1, although this may not be valid for inner disks. The gas mass within the warp is then roughly estimated by

$$M_{warp,gas} = 1.5 \times 10^{21} \times A_V \times m_H \times S_{warp}, \quad (3)$$

where  $m_H$  is the atomic mass of hydrogen and  $S_{warp}$  represents the cross-section area of the warp. We infer from the light curve that the warps have a Gaussian shape with a central height  $H = 2 R_*$ . The estimated gas mass is  $1.6 \times 10^{20} \text{ g}$  for warps with an average extinction of  $A_V = 1 \text{ mag}$ . The short-duration extinction events in 2015–2016 are less deep and would therefore either have less mass or a lower scale height.

#### 4.2. The Extinction Curve of the Dips of GI Tau

Extinction events in single-band photometry have degenerate explanations: the star may be entirely occulted by dust described by some column density and extinction law, or a fraction of the star may be entirely occulted by a large column



**Table 4**  
Hours-long Timescale Bursts

Time (MJD-56950)	$\Delta B$ (mag)	$\Delta V$ (mag)	$\Delta I$ (mag)	Duration (hr) <sup>a</sup>	$\dot{M}_{\text{acc,min}}$ <sup>b</sup>	$\dot{M}_{\text{acc,max}}$ <sup>b</sup>
458.7	>0.31	0.32	0.12	2.4	2.27	7.31
461.7	0.04	0.03	0.005	1.0	<sup>c</sup>	<sup>c</sup>
462.6	0.10	0.07	0.02	2.2	8.77	11.1
462.7	0.06	0.02	...	1.7	11.5	14.4
462.8	0.17	0.10	0.10	>1.44	11.6	15.4

**Notes.**

<sup>a</sup> Full duration of bursts measured by  $\Delta B$  in Figure 9.

<sup>b</sup> The mass accretion rates are in units of  $1 \times 10^{-9} M_{\odot} \text{ yr}^{-1}$ .

<sup>c</sup> The  $B$ -band photometry is below the detection limit set in Section 4.3.

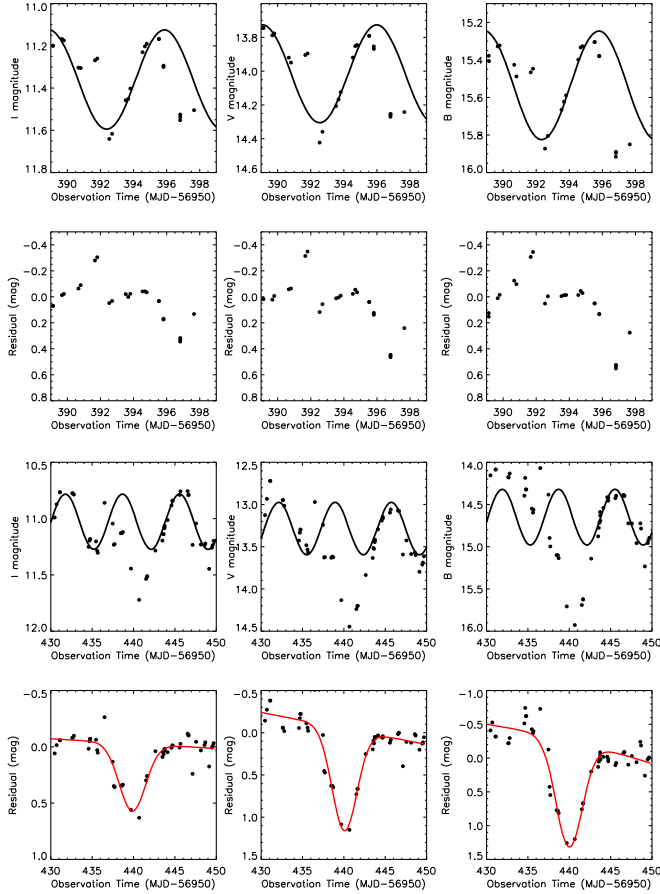


**Figure 8.** Top two panels:  $I$ -,  $V$ -, and  $B$ -band light curves of GI Tau from days 391–399, with sinusoidal fits with the 7.02 day period and residuals from the fit. Curves in the upper panels show the sine fit as spot modulation. Bottom two panels: same as the top set of panels, for days 430–450 and showing a Gaussian profile fit to extinction events in red.

of dust (see discussion in, e.g., Bodman et al. 2017). If the star is entirely occulted by dust, then the wavelength dependence of the extinction will lead to an estimate of grain growth, as long as reflected light is not significant. If only a fraction of the star is covered by opaque dust, then the star will get fainter but the color will not change.

Figure 12 shows the flux-calibrated spectra of GI Tau obtained at minimum brightness during an extinction event and maximum brightness obtained at the end of that event. The ratio of the two spectra demonstrates that GI Tau is much redder during occultation than out of occultation. The TiO band

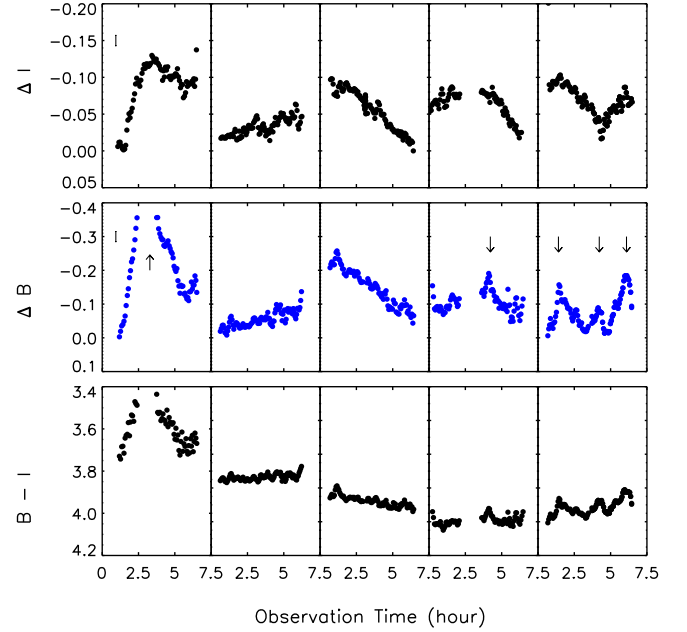


**Figure 9.**  $B$ -,  $I$ -, and  $B - I$  light curves of GI Tau from five consecutive half-nights using NOWT. The  $B$ - and  $I$ -band light curves are normalized to the minimum brightness within each day to compare their morphologies. Strong accretion bursts are marked by arrows. Error bars for the  $B$  and  $I$  bands are shown at the upper-left corner.

ratios and Balmer jumps are similar, indicating that the changes are caused by extinction rather than any change in spot coverage or accretion. The redder spectrum in this epoch is consistent with our other spectra obtained during the same run, the few spectra analyzed by Herczeg & Hillenbrand (2014), and our photometric results.

The flux ratio between 4000 and 8500 Å is fit with an extinction curve from Cardelli et al. (1989), with free parameters  $A_V$  and a total-to-selective extinction  $R_V$  between 2.1 and 5.8. The best-fit  $R_V = 3.85 \pm 0.5$  indicates possible grain growth relative to the ISM. This fit is constrained primarily by flux at  $<5000$  Å. The flux ratio<sup>15</sup> of the spectrum deviates from the fit above 8000 Å for all  $R_V$ . This analysis ignores any contribution from dust scattering, which is likely important at bluer wavelengths (see, e.g., the analysis of AA Tau by Schneider et al. 2015a). The  $V$ -band magnitude of the fainter spectrum is in the range where the “blue turnaround” makes the spectrum appear bluer than one would expect from extinction alone. If considered, scattering

<sup>15</sup> The flux ratio does not include any jump at 8200 Å that could be caused by Paschen absorption in the gas in our line of sight.

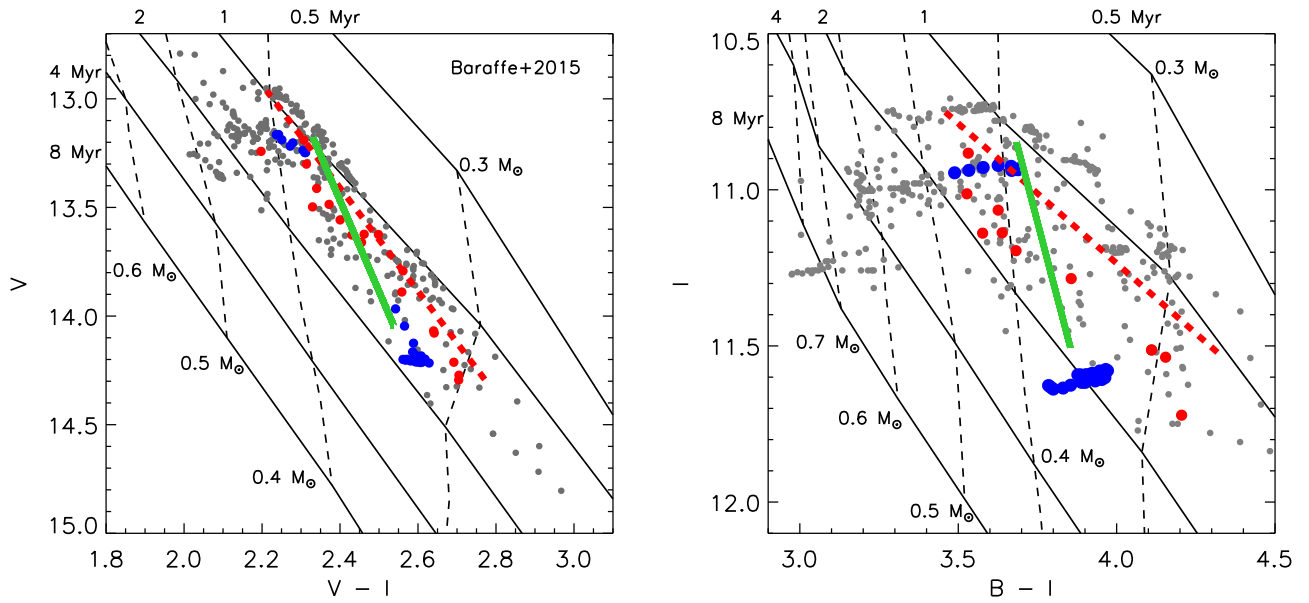


**Figure 10.** Left: the  $V - I$  vs.  $V$  color–magnitude diagram from our multiband monitoring of GI Tau, with observed data from 2015–2016 in gray. Pre-main-sequence evolutionary models by Baraffe et al. (2015) are presented to show the isochrones and mass tracks shifted to a 140 pc distance. The red dots show the extinction event around day 440. The red dashed line shows the fit to the long-time fading event shown in Figure 4. The blue dots are two short accretion bursts detected by NOWT. Spot modulation is shown by the green line. Right: the  $V - I$  vs.  $I$  color–magnitude diagram, with the same points as on the left.

**Table 5**  
Trace on the Color–Magnitude Diagram

Mechanism	$\Delta B$	$\Delta V$	$\Delta R$	$\Delta I$	$\Delta I / \Delta(B - I)$
Spot	0.38	0.32	0.25	0.24	1.71
Accretion	0.20	0.07	0.04	0.02	0.11
Extinction dip <sup>a</sup>	1.56	1.22	...	0.60	0.63
Long term	1.80	1.50	...	0.80	0.80

**Note.**

<sup>a</sup> The extinction dip represents the extinction event centered at day 440.

**Table 6**  
Photometric Period of GI Tau

Year	Period (day)	Amp. $V$ (mag)	Number of Obs.	References
1984	$7.18 \pm 0.05$	0.22	68	a
1987	$7.13 \pm 0.06$	0.34	38	b
1988	$7.01 \pm 0.17$	0.33	45	b
1989	$7.00 \pm 0.06$	0.20	66	b
1990	$7.06 \pm 0.05$	0.35	57	b
1991	$7.28 \pm 0.18$	0.40	31	b
1992	$7.33 \pm 0.14$	0.47	24	b
1993	...	1.64	35	b
2003	...	0.60	9	c
2014	(21)	2.20	174	d
2015	$7.03 \pm 0.02$	0.26	324	d

**Note.** The periods listed in this table are photometric periods of GI Tau. In this work, we claim that the  $\sim 7$  day periods are close to the stellar spin and the 21 day period is an obscuration period contributed by the “slow warp” located outside the inner edge of circumstellar disk. The Amp.  $V$  here is the amplitude of the sinusoidal fit from the Generalized Lomb–Scargle (GLS) periodogram and does not represent the obscuration depth. In the years 1993 and 2003, there is no period detected from the periodicity analysis.

**References:** (a) Vrba et al. (1986), (b) Herbst et al. (1994), (c) Grankin et al. (2007), (d) this work.

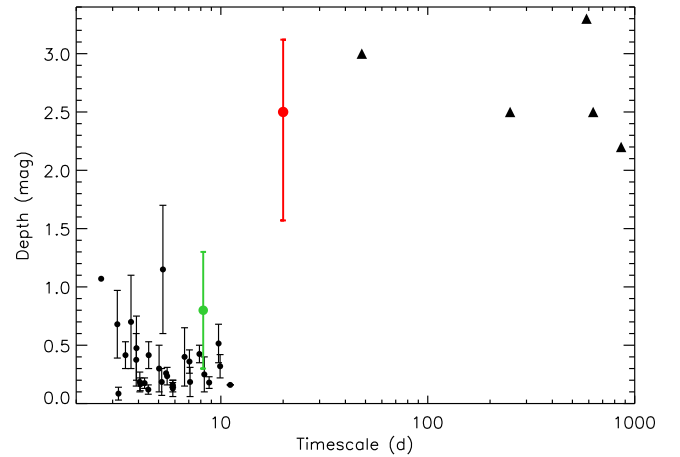


**Figure 11.** Depth and timescale for extinction events of classical T Tauri stars, with the 2014–2015 quasi-periodicity and the months-long extinction from late 2015 shown in red. Periodic or quasi-periodic targets from McGinnis et al. (2015), Stauffer et al. (2015), and Ansdell et al. (2016b) are shown as circles and cluster at periods consistent with stellar rotation and extinctions of 0.1–1 mag. Periodic variation of AA Tau is marked in green. Long-term extinction events of the faders KH 15D, RW Aur, V409 Tau, and DM Ori from Kearns & Herbst (1998) and Rodríguez et al. (2015, 2016b) are shown by triangles and plotted with “timescale” indicating the duration of the event. These extinction events are usually deeper, though this may be an observational bias.

would lead to a lower  $R_V$  and may also explain the deviation at red wavelengths. If some fraction of the star is covered by a much higher dust extinction, then  $R_V$  would need to be much lower for the visible fraction of the star.

Diffuse interstellar bands (see the review by Herbig 1995) are not detected in any spectrum, but would be expected to be strong if the dust composition were similar to the ISM (Friedman et al. 2011). These bands are strong in lines of sight through molecular clouds (e.g., Vos et al. 2011), and when seen in the spectra of some young stars (e.g., Oudmaijer et al. 1997;

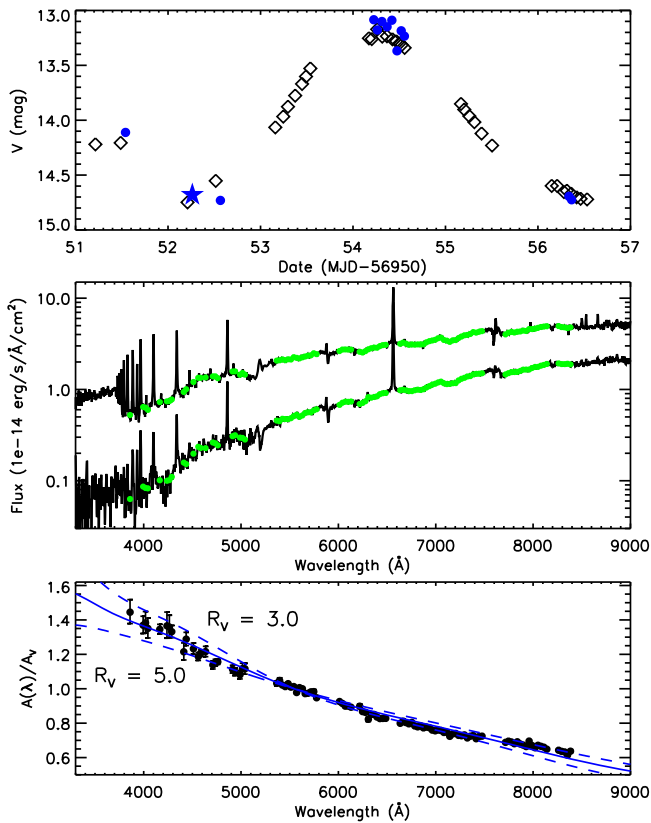


**Figure 12.** Top: Bessell  $V$ -band light curve of GI Tau during the SNIFS survey. The photometry by acquisition images are shown by the black diamonds, while the blue dots and stars are the synthetic photometry obtained from our flux-calibrated spectra. Middle: two SNIFS spectra of GI Tau, with one obtained during a bright epoch on day 54 and one obtained during a faint epoch on day 52 (both marked as stars above). The green dots mark the locations of the spectra used to measure the extinction law. Bottom: extinction law (flux ratio) of the spectra shown in the middle panel, normalized by  $A(\lambda)$  at  $5500 \text{ \AA}$ . The blue lines show the reddening curves of Cardelli et al. (1989) for  $R_V = 3.85$  (solid) and 3.0 and 5.0 (dotted).

Rodgers et al. 2002) are likely caused by the interstellar medium rather than the disk. Dust heating and processing within the disk of GI Tau must have destroyed the complex molecules that cause these bands. This difference could provide a method to distinguish disk extinction from interstellar extinction.

The flux in the  $[\text{O I}] 6300 \text{ \AA}$  emission does not change between epochs, despite the change in extinction. High-resolution spectra of GI Tau include broad and narrow components (e.g., Simon et al. 2016). The bulk of this emission must originate above the star, where the outflow would not be occulted by an inner disk warp.

The wavelength-dependent ratio of the two spectra is consistent with that of the other spectra obtained during the rise from days 52–54. The Balmer jump and therefore the accretion changes between days 54–56, so the later spectra are not immediately useful for  $R_V$  calculations. On the other hand, when calculated from our photometry of extinction events (see Table 5), we obtained  $R_V = A_V / (A_B - A_V) \sim 5$  for the long-term extinction (fader), and the dip in day 440 (dipper) yields  $R_V = 3.6$ . The fits to the long-term fade may be less reliable because they include different points for each band and cover accretion bursts and spot rotation.

The  $R_V$  measurement indicates a low opacity of the obscuration source, in contrast to previous interpretations that

the periodic dips of AA Tau are optically thick (Bouvier et al. 2003). Any optically thin dust in the accretion flow or at the inner disk edge should be quickly destroyed by strong stellar irradiation. In MHD simulations, the accretion stream drags dust grains from the optically thick disk (Romanova et al. 2003), which may replenish the dust in our line of sight. However, the occultation timescales of the dips (e.g., 5 days) are relatively long compared with the crossing timescale of an inner disk warp at the co-rotation radius. Alternative explanations, such as the dust being located in disk winds at larger radii, rather than in the disk itself, could explain the long survival time of the dust (Bans & Königl 2012; Petrov et al. 2015, 2017).

### 4.3. Accretion on Different Timescales

Mass accretion rates ( $\dot{M}_{\text{acc}}$ ) are measured here by calculating the excess continuum and line emission produced by the accretion flow. Our  $B$ -band and limited  $U$ -band monitoring of 2015–2016 are shown in Figure 4, with variations caused by changes in accretion, extinction, and spot coverage. Because scattered light during deep extinction events strongly affects the colors (the “blue turnaround”), accretion rates are calculated only for epochs when  $V < 14.0$  mag.

To measure the excess  $U$ -band luminosity, we first remove the spot modulation effects by a 7.03 day sinusoidal light curve. We then extract the extinction-corrected photospheric emission from the flux-calibrated optical spectra of Herczeg & Hillenbrand (2014). The combined fit of a photospheric template and accretion continuum to the spectrum yields photospheric luminosities of  $U_{\text{photosphere}} = 14.54 \pm 0.1$  mag,  $B_{\text{photosphere}} = 13.44 \pm 0.05$  mag, and  $I_{\text{photosphere}} = 10.43 \pm 0.05$  mag, when corrected to  $A_V = 0$  mag. Any extinction-corrected  $U$ -band emission above this brightness is attributed to accretion. The color of accretion is calculated as  $U - I \sim 0.15$  mag, using assumptions for the accretion continuum from Herczeg & Hillenbrand (2014), as estimated from veiling measurements of Fischer et al. (2011). The color variations are then calculated for a variable extinction, following the  $R_V = 3.85$  curve from Cardelli et al. (1989) with  $A_U = 1.47 A_V$ ,  $A_B = 1.25 A_V$ , and  $A_I = 0.56 A_V$ . Figure 13 shows how extinction and accretion affect the  $U - B$  and  $I$ -band magnitude of GI Tau.

The optical spectral energy distributions of the spot- and extinction-removed examples are presented in Figure 14. The accretion excess usually contributes  $\sim 60\%$  of the emission in the  $U$ -band filter but only  $\sim 15\%$  of the emission in the  $B$ -band filter on the median mass accretion rate  $\dot{M}_{\text{acc}} = 1 \sim 4 \times 10^{-9} M_{\odot} \text{ yr}^{-1}$ , consistent with expectations from accretion models (e.g., Calvet & Gullbring 1998). A similar relationship is seen by comparing the left and right panels of Figure 13 where the data points are more scattered in  $U$ .

Following the empirical relationship from Gullbring et al. (1998),  $\log(L_{\text{acc}}/L_{\odot}) = 1.09^{+0.04}_{-0.18} \log(L_U^{\text{ex}}/L_{\odot}) + 0.98^{+0.02}_{-0.07}$ , the accretion luminosity of GI Tau is calculated using the  $U$ -band accretion luminosity,  $L_{\text{acc}}$ , from

$$L_U^{\text{acc}} = 4\pi d^2 F_{\text{zeropoint}} \times (10^{-0.4U_{\text{unred}}} - 10^{-0.4U_{\text{photosphere}}}), \quad (4)$$

where  $F_{\text{zeropoint}}$  is the zero point of the generic  $U$  band, the distance  $d = 140$  pc, and  $U_{\text{unred}}$  is the spot modulation and extinction reddening removed  $U$  magnitude. The accretion luminosity ranges from  $\sim 0$  to  $41 \times 10^{-2} L_{\odot}$ . The accretion

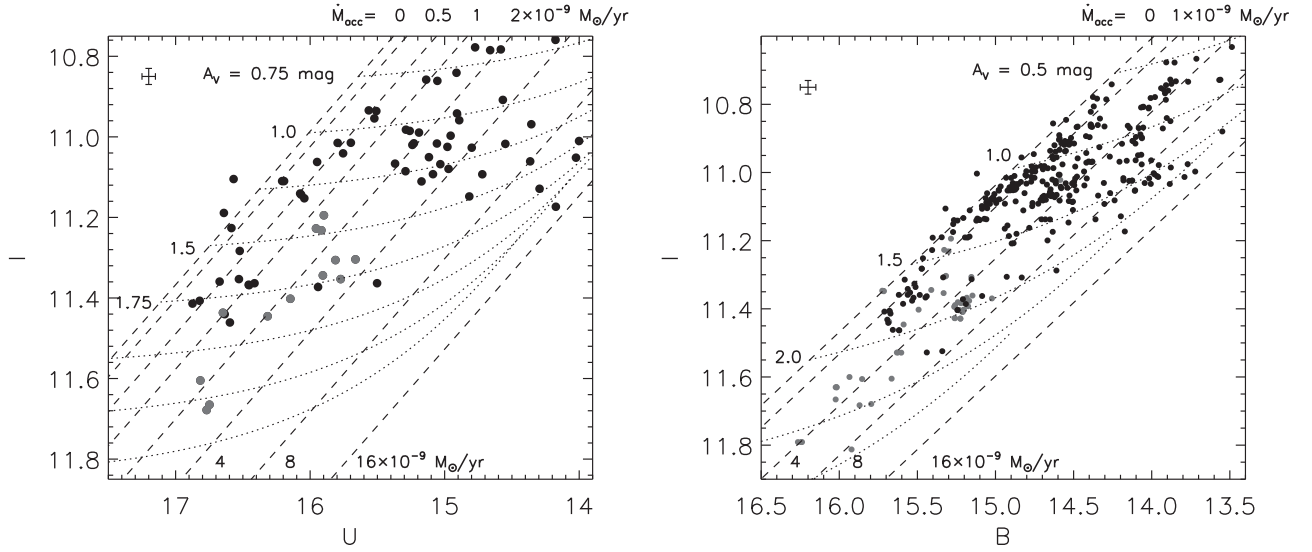


**Figure 13.** Spot-corrected  $U$  vs.  $I$  (left) and  $B$  vs.  $I$  (right) during our 2015–2016 monitoring of GI Tau. The spots are removed as sinusoidal light curves with parameters in Table 2. This grid is calculated based on two assumptions: (a)  $I = U - 0.15$  as the accretion and (b) extinction amplitudes in each band follow the  $R_V = 3.85$  curve from Cardelli et al. (1989). The estimated extinction ranges from  $A_V = 0.5$  to 2.5 mag assuming out of extinction brightness  $I = 10.43$  mag (Herczeg & Hillenbrand 2014).

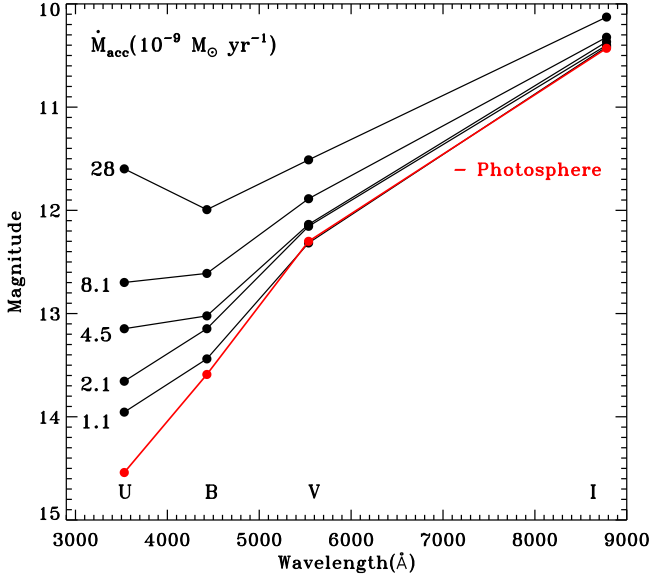


**Figure 14.** Optical spectral energy distributions of GI Tau obtained at five different accretion rates, alongside a photospheric template (red). The photometry has been corrected for extinction. The photospheric template is  $U_{\text{photosphere}} = 14.54$  mag,  $B_{\text{photosphere}} = 13.59$  mag,  $V_{\text{photosphere}} = 12.29$  mag, and  $I_{\text{photosphere}} = 10.43$  mag.

rate  $\dot{M}_{\text{acc}}$  is then derived from the accretion luminosity,

$$\dot{M}_{\text{acc}} \sim 1.25 L_{\text{acc}} R_* / G M_*, \quad (5)$$

where  $R_*$  and  $M_*$  are the radius and mass of GI Tau. The calculated mass accretion rate of GI Tau ranges from  $\sim(0\text{--}52) \times 10^{-9} M_{\odot} \text{yr}^{-1}$  for stellar parameters  $R_* = 1.7 R_{\odot}$  and  $M_* = 0.53 M_{\odot}$ .

We also develop a method to estimate the accretion rate from  $B$ -band photometry, because our time coverage in  $B$  is more extensive than that in  $U$ . After removing the sinusoidal spot modulation, the extinction and accretion for each  $B$  and  $I$  data point are estimated from the grid shown in Figure 13. The excess  $B$ -band emission produced by accretion is

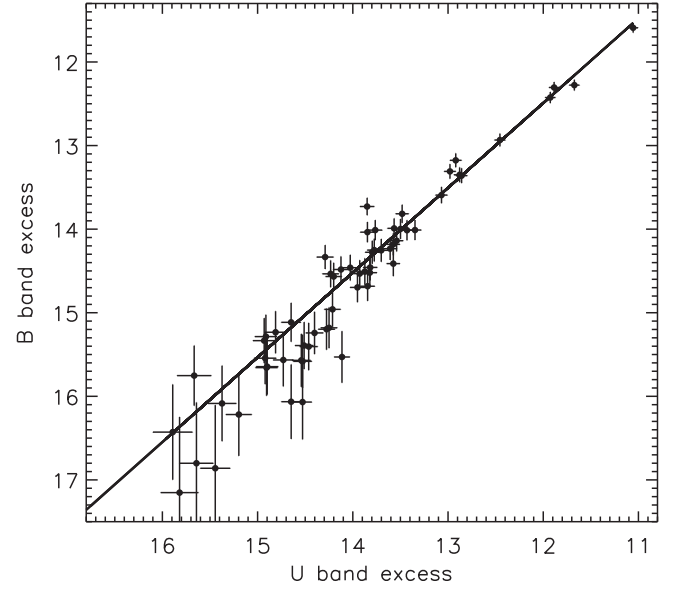


**Figure 15.** Correlation of the  $U$ - and  $B$ -band excess of GI Tau, both generated by accretion. The photometry has been corrected for spots, de-reddened, with an excess then measured against an estimated photospheric magnitude of  $U_{\text{photosphere}} = 14.54$  mag,  $B_{\text{photosphere}} = 13.44$  mag. The best linear fitting result is  $U_{\text{ex}} = 0.93 B_{\text{ex}} + 0.52$ .

calculated from

$$B_{\text{ex}} = -2.5 \log(10^{-0.4B_{\text{unred}}} - 10^{-0.4B_{\text{photosphere}}}), \quad (6)$$

where  $B_{\text{unred}}$  is the de-reddened magnitude in the  $B$  band using the extinction curve of  $R_V = 3.85$ . Figure 15 shows a linear relationship between nearly simultaneous  $U_{\text{ex}}$  and  $B_{\text{ex}}$ , with a best-fit

$$U_{\text{ex}} = 0.93 B_{\text{ex}} + 0.52. \quad (7)$$

The bolometric correction of the  $B$ -band excess is then combined with Equation (7) and the empirical relationship

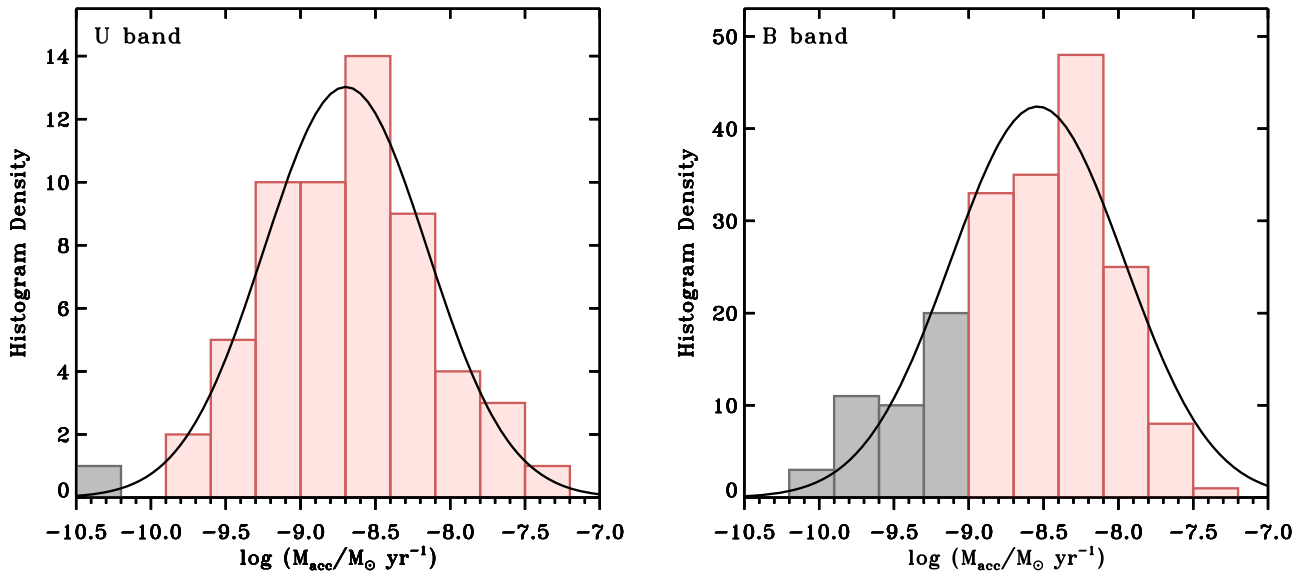


**Figure 16.** Histograms of accretion rates calculated using the  $U$ - (left) and  $B$ -band (right) excess throughout the entire 2015–2016 campaign. The data points taken within 2 hr are binned as one. The mass accretion rates higher and lower than the detection limit are shown in pink and gray, respectively. Gaussian fits of the histograms are shown by thick lines.

given by Gullbring et al. (1998) as

$$\log(L_{\text{acc}}/L_{\odot}) = 1.22_{-0.19}^{+0.05} \log(L_B^{\text{ex}}/L_{\odot}) + 1.46_{-0.10}^{+0.06}. \quad (8)$$

Based on the accuracy of our photometry and the correction for spots, estimated as  $\sim 0.1$  mag in both  $B$  and  $U$  bands, our detection limits of the accretion rate measurement are set as  $\log(M_{\text{acc}}/M_{\odot} \text{ yr}^{-1}) > -9.0$  for the  $B$  band and  $> -10.0$  for the  $U$  band. The correlation between the near-simultaneous  $B$ -band and  $U$ -band accretion rates is tight at rates higher than  $\log(M_{\text{acc}}/M_{\odot} \text{ yr}^{-1}) > -8.2$  but unreliable at lower accretion rates.

The mass accretion rates of GI Tau calculated from  $U$ - and  $B$ -band excesses are summarized in Figure 16. As measured from the  $U$ -band excess, the 5th to 95th percentile range of  $\log(M_{\text{acc}}/M_{\odot} \text{ yr}^{-1})$  is  $-7.89$  to  $-9.77$ , with a center at  $-8.70$  and sigma of 0.53 dex in the Gaussian fit. These results are consistent with results from the more extensive  $B$ -band photometry, which yielded an average  $\log M_{\text{acc}}/M_{\odot} \text{ yr}^{-1} = -8.55$  with 0.6 dex scatter. These estimates are obtained by creating mock sets of accretion rates over a range of values for the average and standard deviations and assuming a Gaussian distribution and upper limits. The adopted values are then obtained from maximizing the probability from a Kolmogorov–Smirnov test between the observed distribution and each mock data set. The distribution of  $B$ -band accretion rates includes the NOWT data sampled at a time resolution of one hour. The best-fit  $B$ -band data overpredict the number of data points at high accretion rates, as seen in Figure 16. Differences in results between the  $B$ -band and  $U$ -band accretion rates are likely attributable to the large scatter in the  $B$  band at average and weaker accretion rates.

This distribution of accretion rates is consistent with the distribution of accretion rates measured for stars of similar mass (e.g., Fang et al. 2013; Venuti et al. 2014; Manara et al. 2017). However, the distribution demonstrates the importance of accretion bursts in models of disk evolution. The average mass accretion rate of GI Tau is  $4.7 \times 10^{-9} M_{\odot} \text{ yr}^{-1}$ , two times faster than the average inferred from  $\log(M_{\text{acc}}/M_{\odot} \text{ yr}^{-1})$ . Moreover, a total of 50% of the mass is accreted during

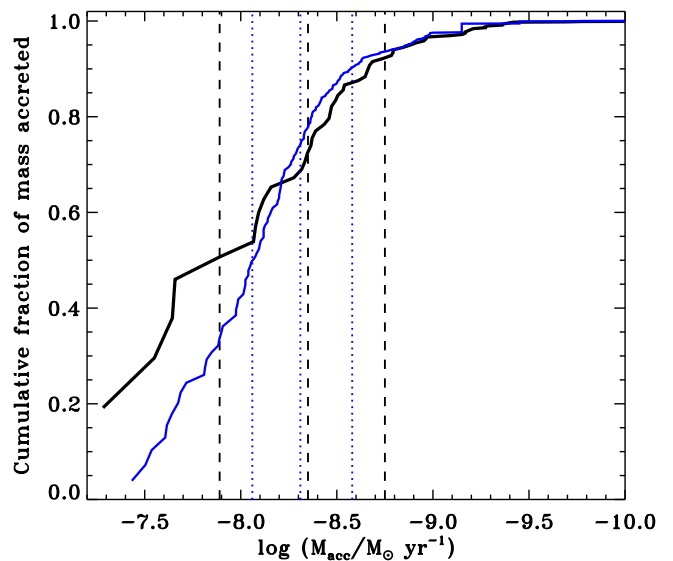


**Figure 17.** Distribution of the mass accretion rate measured using  $U$ - (black) and  $B$ -band (blue) photometry. Vertical dashed/dotted lines from left to right indicate the accretion rate above which half the mass is accreted, the average accretion rate, and the average mass accretion rate in log space.

accretion bursts when the accretion rate is higher than  $12.8 \times 10^{-9} M_{\odot} \text{ yr}^{-1}$  (Figure 17). Such bursts are seen in our high-cadence NOWT monitoring, where, for example, the accretion rate increased from  $\sim 2.3 \times 10^{-9} M_{\odot} \text{ yr}^{-1}$  to  $7.3 \times 10^{-9} M_{\odot} \text{ yr}^{-1}$  over several hours on day 458.

The periods of high accretion deplete most of the disk; the periods of low accretion are irrelevant. However, models of disk evolution (e.g., Rosotti et al. 2016; Lodato et al. 2017; Mulders et al. 2017; Rafikov 2017) assume that the accretion rates are static. Although these distributions cannot be fully explained by variability (Costigan et al. 2014; Venuti et al. 2015) and surely include some stars that are strong accretors and others that are weak, bursts should be expected to play a significant role in the mass accretion. The distribution of high accretion rates could also be in excess over a Gaussian

distribution. Future analyses should incorporate time-averaged accretion rates (e.g., Venuti et al. 2015) over many epochs and perhaps even many years.

## 5. Conclusions

Our two-year multiband photometric monitoring of the classical T Tauri star GI Tau revealed variability caused by extinction, accretion, and spots, each with unique signatures in color–magnitude diagrams. The deep extinction events of  $\Delta V = 2\text{--}3$  mag were seemingly stochastic in their timing and duration, with some occultations lasting 3–5 days and one 80 day-long dimming. During three months in 2014–2015, the short dips recurred with a quasi-period of  $\sim 21$  days, as might be expected from the sub-Keplerian slow warp seen in the simulations of Romanova et al. (2013). The stellar rotation period of  $7.03 \pm 0.02$  days is recovered from the second half of the 2015–2016 light curve but is not apparent in our earlier light curve, consistent with previous period estimates from some epochs (see Table 6) and with an inability to recover that period in other epochs.










A wavelength-dependent extinction curve is fitted by spectral ratios, with best-fit  $R_V = 3.85 \pm 0.5$ . Diffuse interstellar bands are not detected from the spectra. The average mass accretion rate of GI Tau of  $\sim 4.7 \times 10^{-9} M_\odot \text{yr}^{-1}$  is calculated from excess *U*- and *B*-band light curves, after accounting for extinction and spots. The distribution of accretion rates demonstrates that most of the accretion occurs during bursts, so the quiescent accretion rates may provide a misleading evaluation of accretion as a diagnostic of disk physics.

We thank the anonymous referee for helpful comments and suggestions that improved the clarity and robustness of the results. Z.G. thanks Prof. Douglas N. C. Lin for helpful discussions. We also thank Hiro Takami, Stefano Facchini, and Carlo Manara for discussions on RW Aur, and Petr Petrov for discussions on extinction in disk winds. We also thank all of the observers and staff who contributed to this project, including those at the HCT (operated by the Indian Institute of Astrophysics), YNAO, VBO, TNO, HCT, and Lulin observatories.

We thank Guojie Feng, Chunhai Bai, Shuguo Ma, Guangxin Pu, Abususaimaitijiang Yisikandeer, and Xuan Zhang from Xingjiang Astronomical Observatory for organizing and running the NOWT observations that are partially supported by the CAS “Light of West China” program (2015-XBQN-A-02).

Z.G., G.J.H., and J.J. are supported by general grant 11473005 awarded by the National Science Foundation of China. J.N.F. acknowledges the support from the National Natural Science Foundation of China (NSFC) through grant 11673003 and the National Basic Research Program of China (973 Program 2014CB845700 and 2013CB834900).

## ORCID iDs

Zhen Guo  <https://orcid.org/0000-0003-0292-4832>  
 Gregory J. Herczeg  <https://orcid.org/0000-0002-7154-6065>  
 Jianning Fu  <https://orcid.org/0000-0001-8241-1740>  
 Po-Shih Chiang  <https://orcid.org/0000-0003-3167-2523>  
 Raúl Michel  <https://orcid.org/0000-0003-1263-808X>  
 Ram Kesh Yadav  <https://orcid.org/0000-0002-6740-7425>  
 Wen-ping Chen  <https://orcid.org/0000-0003-0262-272X>  
 Saurabh Sharma  <https://orcid.org/0000-0001-5731-3057>  
 Angel Castro  <https://orcid.org/0000-0002-7832-5337>

## References

- Aldering, G., Adam, G., Antilogus, P., et al. 2002, *Proc. SPIE*, 4836, 61  
 Alencar, S. H. P., Bouvier, J., Walter, F. M., et al. 2012, *A&A*, 541, A116  
 Alencar, S. H. P., Teixeira, P. S., Guimarães, M. M., et al. 2010, *A&A*, 519, A88  
 Allard, F. 2014, in IAU Symp. vol 299, Exploring the Formation and Evolution of Planetary Systems, ed. M. Booth, B. C. Matthews, & J. R. Graham (Cambridge: Cambridge Univ. Press), 271  
 Ansdell, M., Gaidos, E., Rappaport, S. A., et al. 2016b, *ApJ*, 816, 69  
 Ansdell, M., Gaidos, E., Williams, J. P., et al. 2016a, *MNRAS*, 462, L101  
 Arce, H. G., & Sargent, A. I. 2006, *ApJ*, 646, 1070  
 Audard, M., Briggs, K. R., Grosso, N., et al. 2007, *A&A*, 468, 379  
 Bans, A., & Königl, A. 2012, *ApJ*, 758, 100  
 Baraffe, I., Homeier, D., Allard, F., & Chabrier, G. 2015, *A&A*, 577, A42  
 Beccari, G., Bellazzini, M., Magrini, L., et al. 2017, *MNRAS*, 465, 2189  
 Blinova, A. A., Romanova, M. M., & Lovelace, R. V. E. 2016, *MNRAS*, 459, 2354  
 Bodman, E. H. L., Quillen, A. C., Ansdell, M., et al. 2017, *MNRAS*, 470, 202  
 Bohlin, R. C., Savage, B. D., & Drake, J. F. 1978, *ApJ*, 224, 132  
 Bouvier, J., Alencar, S. H. P., Boutelier, T., et al. 2007, *A&A*, 463, 1017  
 Bouvier, J., Chelli, A., Allain, S., et al. 1999, *A&A*, 349, 619  
 Bouvier, J., Grankin, K., Ellerbroek, L. E., Bouy, H., & Barrado, D. 2013, *A&A*, 557, A77  
 Bouvier, J., Grankin, K. N., Alencar, S. H. P., et al. 2003, *A&A*, 409, 169  
 Calvet, N., & Gullbring, E. 1998, *ApJ*, 509, 802  
 Camenzind, M. 1990, *RvMA*, 3, 234  
 Cardelli, J. A., Clayton, G. C., & Mathis, J. S. 1989, *ApJ*, 345, 245  
 Cody, A. M., Hillenbrand, L. A., David, T. J., et al. 2017, *ApJ*, 836, 41  
 Cody, A. M., Stauffer, J., Baglin, A., et al. 2014, *AJ*, 147, 82  
 Cohen, M., & Kuhl, L. V. 1979, *ApJS*, 41, 743  
 Costigan, G., Vink, J. S., Scholz, A., Ray, T., & Testi, L. 2014, *MNRAS*, 440, 3444  
 Daemgen, S., Bonavita, M., Jayawardhana, R., Lafrenière, D., & Janson, M. 2015, *ApJ*, 799, 155  
 Dai, F., Facchini, S., Clarke, C. J., & Haworth, T. J. 2015, *MNRAS*, 449, 1996  
 Donati, J.-F., & Landstreet, J. D. 2009, *ARA&A*, 47, 333  
 Dullemond, C. P., van den Ancker, M. E., Acke, B., & van Boekel, R. 2003, *ApJL*, 594, L47  
 Espaillat, C., Furlan, E., D’Alessio, P., et al. 2011, *ApJ*, 728, 49  
 Facchini, S., Manara, C. F., Schneider, P. C., et al. 2016, *A&A*, 596, A38  
 Fang, M., Kim, J. S., van Boekel, R., et al. 2013, *ApJS*, 207, 5  
 Feiden, G. A. 2016, arXiv:1604.08036  
 Findeisen, K., Hillenbrand, L., Ofek, E., et al. 2013, *ApJ*, 768, 93  
 Fischer, W., Edwards, S., Hillenbrand, L., & Kwan, J. 2011, *ApJ*, 730, 73  
 Fischer, W., Kwan, J., Edwards, S., & Hillenbrand, L. 2008, *ApJ*, 687, 1117  
 Friedman, S. D., York, D. G., McCall, B. J., et al. 2011, *ApJ*, 727, 33  
 Grankin, K. N. 2016, *AstL*, 42, 314  
 Grankin, K. N., Bouvier, J., Herbst, W., & Melnikov, S. Y. 2008, *A&A*, 479, 827  
 Grankin, K. N., Melnikov, S. Y., Bouvier, J., Herbst, W., & Shevchenko, V. S. 2007, *A&A*, 461, 183  
 Grinin, V. P. 1988, *SvAL*, 14, 27  
 Grinin, V. P., Kiselev, N. N., Chernova, G. P., Minikulov, N. K., & Voshchinnikov, N. V. 1991, *Ap&SS*, 186, 283  
 Grinin, V. P., The, P. S., de Winter, D., et al. 1994, *A&A*, 292, 165  
 Gullbring, E., Hartmann, L., Briceño, C., & Calvet, N. 1998, *ApJ*, 492, 323  
 Gully-Santiago, M. A., Herczeg, G. J., Czekala, I., et al. 2017, *ApJ*, 836, 200  
 Hamilton, C. M., Herbst, W., Shih, C., & Ferro, A. J. 2001, *ApJL*, 554, L201  
 Hartigan, P., Strom, K. M., & Strom, S. E. 1994, *ApJ*, 427, 961  
 Hartmann, L., Herczeg, G., & Calvet, N. 2016, *ARA&A*, 54, 135  
 Herbig, G. H. 1977, *ApJ*, 214, 747  
 Herbig, G. H. 1995, *ARA&A*, 33, 19  
 Herbst, W., Herbst, D. K., Grossman, E. J., & Weinstein, D. 1994, *AJ*, 108, 1906  
 Herczeg, G. J., & Hillenbrand, L. A. 2014, *ApJ*, 786, 97  
 Ingleby, L., Espaillat, C., Calvet, N., et al. 2015, *ApJ*, 805, 149  
 Johns-Krull, C. M. 2007, *ApJ*, 664, 975  
 Johns-Krull, C. M., & Valenti, J. A. 2001, *ApJ*, 561, 1060  
 Jose, J., Kim, J. S., Herczeg, G. J., et al. 2016, *ApJ*, 822, 49  
 Ke, T. T., Huang, H., & Lin, D. N. C. 2012, *ApJ*, 745, 60  
 Kearns, K. E., & Herbst, W. 1998, *AJ*, 116, 261  
 Kenyon, S. J., Gómez, M., & Whitney, B. A. 2008, in Handbook of Star Forming Regions, Vol. I: The Northern Sky, ed. B. Reipurth (San Francisco, CA: ASP), 405

- Kenyon, S. J., & Hartmann, L. 1995, *ApJS*, **101**, 117
- Kesseli, A. Y., Petkova, M. A., Wood, K., et al. 2016, arXiv:1607.00385
- Koenigl, A. 1991, *ApJL*, **370**, L39
- Kowalski, A. F., Mathioudakis, M., Hawley, S. L., et al. 2016, *ApJ*, **820**, 95
- Kraus, A. L., & Hillenbrand, L. A. 2009, *ApJ*, **704**, 531
- Landolt, A. U. 1992, *AJ*, **104**, 340
- Lantz, B., Aldering, G., Antilogus, P., et al. 2004, *Proc. SPIE*, **5249**, 146
- Linnell Nemeč, A. F., & Nemeč, J. M. 1985, *AJ*, **90**, 2317
- Liu, J., Zhang, Y., Feng, G., & Bai, C. 2014, in IAU Symp. 298, Setting the scene for Gaia and LAMOST, ed. S. Feltzing et al. (Cambridge: Cambridge Univ. Press), 427
- Lodato, G., Scardoni, C. E., Manara, C. F., & Testi, L. 2017, arXiv:1708.09467
- Loinard, L., Torres, R. M., Mioduszewski, A. J., et al. 2007, *ApJ*, **671**, 546
- Loomis, R. A., Öberg, K. I., Andrews, S. M., & MacGregor, M. A. 2017, *ApJ*, **840**, 23
- Luhman, K. L., Allen, P. R., Espaillat, C., Hartmann, L., & Calvet, N. 2010, *ApJS*, **186**, 111
- Manara, C. F., Testi, L., Herczeg, G. J., et al. 2017, arXiv:1704.02842
- McGinnis, P. T., Alencar, S. H. P., Guimarães, M. M., et al. 2015, *A&A*, **577**, A11
- Morales-Calderón, M., Stauffer, J. R., Hillenbrand, L. A., et al. 2011, *ApJ*, **733**, 50
- Mulders, G. D., Pascucci, I., Manara, C. F., et al. 2017, arXiv:1708.09464
- Myers, P. C. 1982, *ApJ*, **257**, 620
- Natta, A., Grinin, V. P., Mannings, V., & Ungerechts, H. 1997, *ApJ*, **491**, 885
- Nguyen, D. C., Brandeker, A., van Kerkwijk, M. H., & Jayawardhana, R. 2012, *ApJ*, **745**, 119
- Nguyen, D. C., Scholz, A., van Kerkwijk, M. H., Jayawardhana, R., & Brandeker, A. 2009, *ApJL*, **694**, L153
- Oke, J. B. 1990, *AJ*, **99**, 1621
- Oudmajer, R. D., Busfield, G., & Drew, J. E. 1997, *MNRAS*, **291**, 797
- Padgett, D. L., Brandner, W., Stapelfeldt, K. R., et al. 1999, *AJ*, **117**, 1490
- Petrov, P. P., Babina, E. V., & Artemenko, S. A. 2017, in ASP Conf. Ser. 510, Stars: From Collapse to Collapse, ed. Y. Y. Balega et al. (San Francisco, CA: ASP), 94
- Petrov, P. P., Gahm, G. F., Djupvik, A. A., et al. 2015, *A&A*, **577**, A73
- Rafikov, R. R. 2017, *ApJ*, **837**, 163
- Rebull, L. M., Padgett, D. L., McCabe, C.-E., et al. 2010, *ApJS*, **186**, 259
- Rebull, L. M., Stauffer, J. R., Bouvier, J., et al. 2016, *AJ*, **152**, 113
- Reggiani, M., Robberto, M., Da Rio, N., et al. 2011, *A&A*, **534**, A83
- Robinson, C. E., Owen, J. E., Espaillat, C. C., & Adams, F. C. 2017, *ApJ*, **838**, 100
- Rodgers, B., Wooden, D. H., Grinin, V., Shakhovskiy, D., & Natta, A. 2002, *ApJ*, **564**, 405
- Rodríguez, J. E., Ansdell, M., Oelkers, R. J., et al. 2017a, *ApJ*, **848**, 97
- Rodríguez, J. E., Pepper, J., Stassun, K. G., et al. 2015, *AJ*, **150**, 32
- Rodríguez, J. E., Pepper, J., & Stassun, K. G. 2016a, in IAU Symp. 314, Young Stars Planets Near the Sun, ed. J. H. Kastner, B. Stelzer, & S. A. Metchev (Cambridge: Cambridge Univ. Press), 167
- Rodríguez, J. E., Reed, P. A., Siverd, R. J., et al. 2016b, *AJ*, **151**, 29
- Rodríguez, J. E., Zhou, G., Cargile, P. A., et al. 2017b, *ApJ*, **836**, 209
- Romanova, M. M., Ustyugova, G. V., Koldoba, A. V., & Lovelace, R. V. E. 2013, *MNRAS*, **430**, 699
- Romanova, M. M., Ustyugova, G. V., Koldoba, A. V., Wick, J. V., & Lovelace, R. V. E. 2003, *ApJ*, **595**, 1009
- Rosotti, G. P., Juhasz, A., Booth, R. A., & Clarke, C. J. 2016, *MNRAS*, **459**, 2790
- Rydgren, A. E., Strom, S. E., & Strom, K. M. 1976, *ApJS*, **30**, 307
- Scaringi, S., Manara, C. F., Barenfeld, S. A., et al. 2016, *MNRAS*, **463**, 2265
- Schneider, P. C., France, K., Günther, H. M., et al. 2015a, *A&A*, **584**, A51
- Schneider, P. C., Günther, H. M., Robrade, J., et al. 2015b, *A&A*, **584**, L9
- Shu, F., Najita, J., Ostriker, E., et al. 1994, *ApJ*, **429**, 781
- Sicilia-Aguilar, A., Hartmann, L. W., Hernández, J., Briceño, C., & Calvet, N. 2005, *AJ*, **130**, 188
- Simon, M., Guilloteau, S., Di Folco, E., et al. 2017, *ApJ*, **844**, 158
- Simon, M. N., Pascucci, I., Edwards, S., et al. 2016, *ApJ*, **831**, 169
- Sousa, A. P., Alencar, S. H. P., Bouvier, J., et al. 2016, *A&A*, **586**, A47
- Stauffer, J., Cody, A. M., Baglin, A., et al. 2014, *AJ*, **147**, 83
- Stauffer, J., Cody, A. M., McGinnis, P., et al. 2015, *AJ*, **149**, 130
- Stauffer, J., Cody, A. M., Rebull, L., et al. 2016, *AJ*, **151**, 60
- Taguchi, Y., Itoh, Y., & Mukai, T. 2009, *PASJ*, **61**, 251
- Takami, M., Wei, Y.-J., Chou, M.-Y., et al. 2016, *ApJ*, **820**, 139
- Tofflemire, B. M., Mathieu, R. D., Ardila, D. R., et al. 2017a, *ApJ*, **835**, 8
- Tofflemire, B. M., Mathieu, R. D., Herczeg, G. J., Akeson, R. L., & Ciardi, D. R. 2017b, *ApJL*, **842**, L12
- Torres, R. M., Loinard, L., Mioduszewski, A. J., et al. 2012, *ApJ*, **747**, 18
- Torres, R. M., Loinard, L., Mioduszewski, A. J., & Rodríguez, L. F. 2009, *ApJ*, **698**, 242
- Valenti, J. A., Basri, G., & Johns, C. M. 1993, *AJ*, **106**, 2024
- Venuti, L., Bouvier, J., Flaccomio, E., et al. 2014, *A&A*, **570**, A82
- Venuti, L., Bouvier, J., Irwin, J., et al. 2015, *A&A*, **581**, A66
- Vos, D. A. I., Cox, N. L. J., Kaper, L., Spaans, M., & Ehrenfreund, P. 2011, *A&A*, **533**, A129
- Vrba, F. J., Rydgren, A. E., Chugainov, P. F., Shakovskaia, N. I., & Zak, D. S. 1986, *ApJ*, **306**, 199
- Wenzel, W. 1969, *MitVS*, **5**, 75
- Zajtseva, G. V. 2010, *Ap*, **53**, 212
- Zechmeister, M., & Kürster, M. 2009, *A&A*, **496**, 577
- Zhang, K., Blake, G. A., & Bergin, E. A. 2015, *ApJL*, **806**, L7